

The physics of ghost imaging

Jeffrey H. Shapiro · Robert W. Boyd

Received: 25 October 2011 / Accepted: 30 December 2011 / Published online: 14 January 2012
© Springer Science+Business Media, LLC 2012

Abstract Ghost images are obtained by correlating the output of a single-pixel (bucket) photodetector—which collects light that has been transmitted through or reflected from an object—with the output from a high spatial-resolution scanning photodetector or photodetector array whose illumination has not interacted with that object. The term “ghost image” is apt because neither detector’s output alone can yield an image: the bucket detector has no spatial resolution, while the high spatial-resolution detector has not viewed the object. The first ghost imaging experiment relied on the entangled signal and idler outputs from a spontaneous parametric downconverter, and hence the image was interpreted as a quantum phenomenon. Subsequent theory and experiments showed, however, that classical correlations can be used to form ghost images. For example, ghost images can be formed with pseudothermal light, for which quantum mechanics is not required to characterize its photodetection statistics. This paper presents an overview of the physics of ghost imaging. It clarifies and unites two disparate interpretations of pseudothermal ghost imaging—two-photon interference and classical intensity-fluctuation correlations—that had previously been thought to be

This work was supported by the U.S. Army Research Office MURI grant W911NF-05-0197.

J. H. Shapiro (✉)
Research Laboratory of Electronics, Massachusetts Institute of Technology, Cambridge,
MA, 02139, USA
e-mail: jhs@mit.edu

R. W. Boyd
Institute of Optics and Department of Physics and Astronomy, University of Rochester, Rochester,
NY, 14627, USA
e-mail: boyd@optics.rochester.edu

R. W. Boyd
Department of Physics, University of Ottawa, Ottawa, ON, K1N 6N5, Canada

conflicting. It also reviews recent work on ghost imaging in reflection, ghost imaging through atmospheric turbulence, computational ghost imaging, and two-color ghost imaging.

Keywords Ghost imaging · Photon statistics · Entanglement · Coherence theory · Atmospheric turbulence

1 Introduction

In 1995, Pittman et al. [1] demonstrated a novel imaging modality that used the entangled signal and idler beams produced by spontaneous parametric downconversion (SPDC). As shown in Fig. 1, the signal beam passed through an imaging lens, an interference filter, an aperture—comprised of slits spelling out “UMBC” in an otherwise opaque screen—followed by a collection lens and a single-pixel photon-counting detector. The idler beam propagated to and through an interference filter and then was collected by a scanning fiber tip coupled to another single-photon detector. Neither detector’s output alone sufficed to image the UMBC pattern: the signal beam passed through the UMBC mask, but its single-pixel detector had no spatial resolution, and the scanning fiber tip provided spatial resolution for its detector, but its illumination had not encountered the UMBC mask. Nevertheless, photon coincidence counting—using the outputs from *both* detectors—produced a UMBC image, as shown in Fig. 2. Subsequent papers dubbed this a ghost image, and it was taken to be a quantum effect, owing to the entangled nature of the signal and idler produced by SPDC.

Pittman et al. [1] concluded that, although they had made use of quantum entanglement to form a ghost image, “it is indeed possible to imagine some type of classical source that could partially emulate this behavior.” Abouraddy et al. [2] subsequently

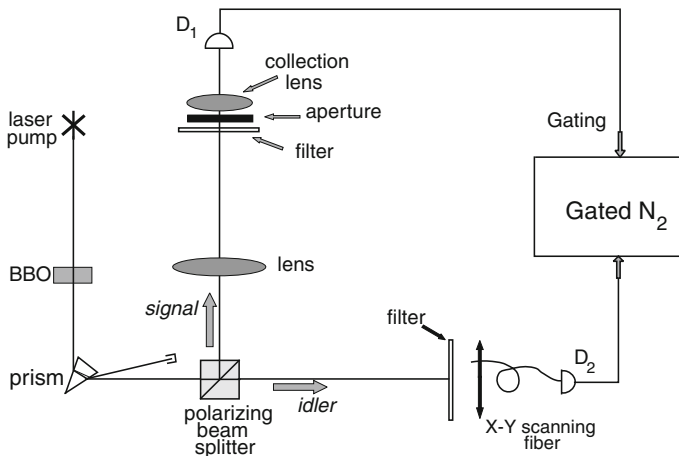


Fig. 1 Schematic setup for the first ghost imaging experiment [1]: BBO is beta-Ba₂BO₄ crystal for spontaneous parametric downconversion; D_1 and D_2 are single-photon detectors; and N_2 is a photon coincidence-counting circuit

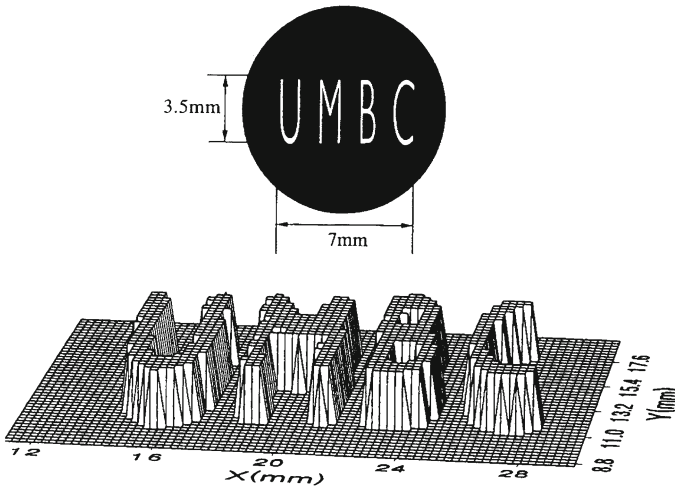


Fig. 2 *Top*: UMBC mask used in the Fig. 1 experiment. *Bottom*: UMBC image obtained from coincidence counting in the Fig. 1 experiment as a function of the fiber tip's transverse coordinates in the image plane. The step size is 0.25 mm, and the image shown is a slice at the half-maximum value

showed, theoretically, that an entangled two-photon source produced a ghost image whose characteristics differed in a fundamental way from those of one obtained using a correlated, but not entangled, two-photon source. Later, Bennink et al. [3] reported an experiment in which a demonstrably classical-state source yielded a ghost image. Gatti et al. [4] followed with a theoretical paper showing that the classical-state setup from [3] could not reproduce a key feature of ghost imaging using an SPDC source: entanglement permits ghost images to be formed in the source's near and far fields. Their result can be understood as follows. According to the rules of quantum mechanics, it is possible to first emit a photon and only after it is already in flight to decide whether to measure its birthplace position or its transverse momentum. The Gatti et al. prediction was confirmed in an experiment performed by Bennink et al. [5], who showed that the same quantum source could form ghost images in either its near or far fields, whereas their classical-state source from [3] could form a ghost image in either its near field or its far field but not both. Howell et al. [6] later showed that the Einstein–Podolsky–Rosen (EPR) correlations of the photons from an SPDC source of the sort used in ghost imaging are strong enough to violate a Reid–EPR [7] bound by a factor of approximately 25.

Still another aspect of ghost imaging emerged when theory [8–11] and experiment [12, 13] showed that pseudothermal light, i.e., laser light that has been rendered spatially incoherent by passage through a rotating ground glass, could be used to form a ghost image, albeit one riding on a significant featureless background level. For example, consider the lensless quasithermal ghost imaging experiment of Scarcelli et al. [14], shown schematically in Fig. 3. Here, light from a pseudothermal (chaotic) source passes through an ordinary beam splitter. One output from this beam splitter illuminates a two-slit transmission mask followed by a bucket detector, while the other

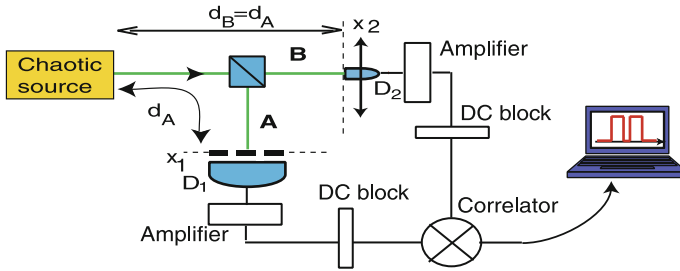


Fig. 3 Schematic setup for the Scarcelli et al. quasithermal lensless ghost imaging experiment [14]; chaotic source is laser light passed through a rotating ground-glass diffuser; D_1 and D_2 are photodiodes; a two-slit mask is placed in front of D_1 ; and the DC block (AC coupling) is used to suppress a featureless background

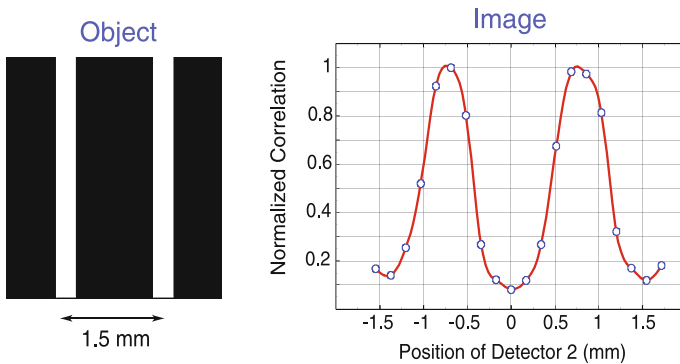


Fig. 4 *Left*: two-slit mask used in the Fig. 3 experiment. *Right*: photocurrent cross correlation as a function of the transverse position of detector D_2

illuminates a scanning detector. Cross correlating the AC-coupled photocurrents from these detectors then yielded the ghost image shown in Fig. 4. Scarcelli et al. provided a quantum-mechanical explanation for their ghost image, showing that it can be understood as resulting from two-photon interference. Furthermore, they claimed that this ghost image could *not* be explained as arising from correlations between the intensity fluctuations in the light beams that illuminate the two detectors in Fig. 3. These assertions have led to considerable controversy. One side argues that the pseudothermal ghost image can be quantitatively explained—with results identical to those obtained from quantum theory—using classical intensity-fluctuation correlations [15, 16]. The other side has argued that nonlocal two-photon interference is the only way to explain the pseudothermal ghost image [14]. In this paper we will end the controversy by clarifying and unifying these competing interpretations.

The remainder of the paper is organized as follows. In Sect. 2 we present brief reviews of some necessary prerequisites: classical and quantum states of light; semiclassical versus quantum photodetection; and coherence propagation for phase-insensitive and phase-sensitive sources.¹ The core of the paper is Sect. 3, which treats

¹ A more extensive review of these topics can be found in [17] and [18].

two forms of far-field lensless ghost-image formation,² one using biphotons (entangled signal-idler photon pairs) obtained from SPDC and the other using pseudo-thermal light. We first reprise the Gaussian-state analyses of ghost images formed with SPDC light [15] and pseudo-thermal light [16]. Here we will use quantum photodetection for the former and semiclassical photodetection for the latter, although the same pseudo-thermal image characteristics have been derived quantum mechanically [15]. Next, in Sect. 4, we probe deeper into the physical interpretation of these ghost images. Both are shown to be consequences of photon-flux-density cross-covariance behavior that, for far-field propagation, is determined by classical coherence propagation, and represents correlations between speckles that illuminate the high-spatial-resolution detector and the object being imaged. Nevertheless, we will see that photocurrent cross-correlation—or photon coincidence counting when flux levels are sufficiently low—leads to a two-photon interference interpretation for *both* the biphoton and pseudo-thermal configurations. In essence, Sect. 4 will close the door on any controversy regarding the physical interpretation of pseudo-thermal ghost-image formation. The quantitatively-identical predictions obtained from the semiclassical and quantum theories of photodetection lead to the speckle cross-correlation and two-photon interference explanations for this process, respectively. That the semiclassical and quantum theories yield identical measurements statistics in this case means that pseudo-thermal ghost-imaging experiments *cannot* distinguish between these two interpretations, even though we know that light is intrinsically quantum mechanical.

Sections 3 and 4 assume single-wavelength operation, a transmissive imaging geometry, and free-space propagation. In Sect. 5 we extend our development to encompass ghost imaging in reflection for single-wavelength operation when there is atmospheric turbulence in the propagation path, thus establishing a foundation for the use of ghost imaging in standoff sensing. Here we draw upon recent experimental [19–21] and theoretical [22–24] work. Section 5 also includes a discussion of computational ghost imaging, in which the ghost image is obtained by correlating the output from a bucket detector with a computed reference field [16,20,21,25,26], as well as two-wavelength operation with an SPDC source [27–29]. We finish, in Sect. 6, with a summary of our essential conclusions, followed by comments about areas for future ghost-imaging research.

2 Preliminaries

Before proceeding to analyses of biphoton and pseudo-thermal ghost imaging, it is important, indeed critical, to establish notation and review essential foundational material. We will be concerned, in Sect. 3, with quasimonochromatic, paraxial, scalar-wave fields at center frequency ω_0 whose nominal propagation direction is along the z axis,

² Whereas the original SPDC ghost imaging setup of Pittman et al., shown in Fig. 1, employed an appropriately-located imaging lens between its light source and the transmission mask, the Scarcelli et al. configuration produces a pseudo-thermal ghost image without such a lens. Thus, to develop a unified understanding of SPDC and pseudo-thermal ghost imaging, in what follows we will consider both source choices only for lensless configurations akin to that in Fig. 3. It should be noted, however, that SPDC ghost imaging has never been demonstrated in a lensless experimental configuration.

and whose transverse coordinate vector is $\boldsymbol{\rho}$. For classical electromagnetic waves we will use $E_z(\boldsymbol{\rho}, t)e^{-i\omega_0 t}$ to denote the $(\text{photons/m}^2\text{s})^{1/2}$ -units positive-frequency field in a constant- z plane.³ In the quantum case, the positive-frequency field operator, $\hat{E}_z(\boldsymbol{\rho}, t)e^{-i\omega_0 t}$, takes the place of this classical field, again with $(\text{photons/m}^2\text{s})^{1/2}$ units. The baseband field operator $\hat{E}_z(\boldsymbol{\rho}, t)$ obeys the following commutation relations [17]

$$[\hat{E}_z(\boldsymbol{\rho}_1, t_1), \hat{E}_z(\boldsymbol{\rho}_2, t_2)] = 0 \tag{1}$$

$$[\hat{E}_z(\boldsymbol{\rho}_1, t_1), \hat{E}_z^\dagger(\boldsymbol{\rho}_2, t_2)] = \delta(\boldsymbol{\rho}_1 - \boldsymbol{\rho}_2)\delta(t_1 - t_2), \tag{2}$$

where $\delta(\cdot)$ is the impulse function. The subsections that follow address: classes of quantum states that will be important for our analysis of ghost imaging; the relation between semiclassical and quantum photodetection; and coherence propagation for phase-insensitive (pseudothermal) and phase-sensitive (biphoton) sources.

2.1 Gaussian states, pseudothermal light, and biphotons

The Gaussian states of the quantized electromagnetic field, $\hat{E}_z(\boldsymbol{\rho}, t)$, are the quantum analogs of classical electromagnetic fields that are Gaussian random processes in space and time. Thus, as in the classical case, they are completely characterized by their first and second moments, i.e., their mean field $\langle \hat{E}_z(\boldsymbol{\rho}, t) \rangle$ and their covariance functions,

$$K_{\hat{E}_z\hat{E}_z}^{(n)}(\boldsymbol{\rho}_1, t_1; \boldsymbol{\rho}_2, t_2) = \langle \Delta \hat{E}_z^\dagger(\boldsymbol{\rho}_1, t_1) \Delta \hat{E}_z(\boldsymbol{\rho}_2, t_2) \rangle \tag{3}$$

$$K_{\hat{E}_z\hat{E}_z}^{(p)}(\boldsymbol{\rho}_1, t_1; \boldsymbol{\rho}_2, t_2) = \langle \Delta \hat{E}_z(\boldsymbol{\rho}_1, t_1) \Delta \hat{E}_z(\boldsymbol{\rho}_2, t_2) \rangle, \tag{4}$$

where $\Delta \hat{E}_z(\boldsymbol{\rho}, t) \equiv \hat{E}_z(\boldsymbol{\rho}, t) - \langle \hat{E}_z(\boldsymbol{\rho}, t) \rangle$. Phase-insensitive field fluctuations are quantified by the normally-ordered covariance, $K_{\hat{E}_z\hat{E}_z}^{(n)}(\boldsymbol{\rho}_1, t_1; \boldsymbol{\rho}_2, t_2)$, because it is invariant to any randomness in the absolute phase of the field. On the other hand, the phase-sensitive covariance, $K_{\hat{E}_z\hat{E}_z}^{(p)}(\boldsymbol{\rho}_1, t_1; \boldsymbol{\rho}_2, t_2)$, is subject to the effect of a random absolute phase.

The coherent state $|E_z(\boldsymbol{\rho}, t)\rangle$ is the quantum analog of the deterministic (noise-free) classical electromagnetic field. It is the eigenket of $\hat{E}_z(\boldsymbol{\rho}, t)$ with eigenfunction $E_z(\boldsymbol{\rho}, t)$:

$$\hat{E}_z(\boldsymbol{\rho}, t)|E_z(\boldsymbol{\rho}, t)\rangle = E_z(\boldsymbol{\rho}, t)|E_z(\boldsymbol{\rho}, t)\rangle, \quad \text{for all } \boldsymbol{\rho}, t. \tag{5}$$

³ These units—chosen for ease of comparison with the quantum case—merely indicate that we are measuring the energy carried by a classical electromagnetic wave in units of $\hbar\omega_0$, rather than in Joules. No quantization is implied at this point.

Equivalently, it is a Gaussian state with $\langle \hat{E}_z(\boldsymbol{\rho}, t) \rangle = E_z(\boldsymbol{\rho}, t)$, $K_{\hat{E}_z \hat{E}_z}^{(n)}(\boldsymbol{\rho}_1, t_1; \boldsymbol{\rho}_2, t_2) = 0$ and $K_{\hat{E}_z \hat{E}_z}^{(p)}(\boldsymbol{\rho}_1, t_1; \boldsymbol{\rho}_2, t_2) = 0$. Because, as we will explain in the next subsection, the quantum photodetection statistics for the coherent state $|E_z(\boldsymbol{\rho}, t)\rangle$ coincide with the semiclassical photodetection statistics for the classical light beam $E_z(\boldsymbol{\rho}, t)$, we say that coherent states are *classical* states. More generally, a quantum state is classical if its quantum photodetection statistics are identical to those obtained from semiclassical photodetection using an appropriate random process $E_z(\boldsymbol{\rho}, t)$. More precisely, the state of $\hat{E}_z(\boldsymbol{\rho}, t)$ is classical if and only if it is a coherent state or a classically-random mixture of coherent states. The latter possibility is saying that $\hat{E}_z(\boldsymbol{\rho}, t)$ is in the coherent state $|E_z(\boldsymbol{\rho}, t)\rangle$, but we have classical uncertainty about its eigenfunction, $E_z(\boldsymbol{\rho}, t)$, so we treat that eigenfunction as a classical random process.

Pseudothermal light is well modeled by a zero-mean Gaussian state whose phase-sensitive covariance vanishes, but whose phase-insensitive (normally-ordered) covariance function is nonzero. All such states are classical [18]. Following prior work on Gaussian-state pseudothermal ghost imaging [15, 18], we shall use the cross-spectrally pure covariance function, $K_{\hat{E}_z \hat{E}_z}^{(n)}(\boldsymbol{\rho}_1, t_1; \boldsymbol{\rho}_2, t_2) = 2\mathcal{K}(\boldsymbol{\rho}_1, \boldsymbol{\rho}_2)\mathcal{R}(t_1 - t_2)$, where the spatial term has the Gaussian-Schell model form

$$\mathcal{K}(\boldsymbol{\rho}_1, \boldsymbol{\rho}_2) = \frac{2P}{\pi a_0^2} e^{-(|\boldsymbol{\rho}_1|^2 + |\boldsymbol{\rho}_2|^2)/a_0^2 - |\boldsymbol{\rho}_1 - \boldsymbol{\rho}_2|^2/2\rho_0^2}, \tag{6}$$

and the temporal term is

$$\mathcal{R}(t_1 - t_2) = e^{-(t_1 - t_2)^2/2T_0^2}, \tag{7}$$

for the phase-insensitive covariance function at the source ($z = 0$) plane, with P being the average photon flux in the signal and reference beams, i.e., after the 50–50 beam splitting employed in pseudothermal lensless ghost imaging. Here: a_0 is the source’s e^{-2} intensity radius; $\rho_0 \ll a_0$ is its spatial coherence length; and T_0 is its coherence time. This is not an exact model for a laser beam that has been passed through a rotating ground-glass diffuser. In particular, the action of the rotating ground-glass diffuser on a continuous-wave laser beam will lead to coupled spatial and temporal variations on the resulting output beam, violating our assumption of cross-spectral purity. Also, our assumption of Gaussian statistics will not be valid until sufficient propagation away from the ground glass has occurred that the Central Limit Theorem can be invoked. Nevertheless, there is little to be lost in employing the preceding statistical model. It is the spatial characteristics that are of primary importance in understanding the physics of ghost imaging. Hence lack of cross-spectral purity is not a major concern. Furthermore, as we shall see in our discussion of coherence theory, pseudothermal ghost imaging is ordinarily done in a far-field regime for which the Central Limit Theorem will apply. More importantly, there is much to be gained by employing the statistical model posited above: the preceding covariance function enables closed-form evaluations of the key performance parameters—field-of-view, spatial resolution, image contrast, and image signal-to-noise ratio—of a lensless pseudothermal ghost image [15, 18, 30–33].

Type-II phase-matched spontaneous parametric downconversion with a continuous wave (cw) pump in the absence of pump depletion produces orthogonally polarized signal and idler beams that are in a maximally-entangled, zero-mean, jointly Gaussian state [34]. When operated at frequency degeneracy, the signal and idler at the source’s output plane can be taken to have positive-frequency field operators $\hat{E}_S(\boldsymbol{\rho}, t)e^{-i\omega_0 t}$ and $\hat{E}_I(\boldsymbol{\rho}, t)e^{-i\omega_0 t}$, for their respective polarizations, whose joint state is completely characterized by the nonzero auto- and cross-covariance functions:

$$K_{SS}^{(n)}(\boldsymbol{\rho}_1, t_1; \boldsymbol{\rho}_2, t_2) \equiv \left\langle \Delta \hat{E}_S^\dagger(\boldsymbol{\rho}_1, t_1) \Delta \hat{E}_S(\boldsymbol{\rho}_2, t_2) \right\rangle, \tag{8}$$

$$K_{II}^{(n)}(\boldsymbol{\rho}_1, t_1; \boldsymbol{\rho}_2, t_2) \equiv \left\langle \Delta \hat{E}_I^\dagger(\boldsymbol{\rho}_1, t_1) \Delta \hat{E}_I(\boldsymbol{\rho}_2, t_2) \right\rangle, \tag{9}$$

$$K_{SI}^{(p)}(\boldsymbol{\rho}_1, t_1; \boldsymbol{\rho}_2, t_2) \equiv \left\langle \Delta \hat{E}_S(\boldsymbol{\rho}_1, t_1) \Delta \hat{E}_I(\boldsymbol{\rho}_2, t_2) \right\rangle. \tag{10}$$

The signal and idler, as individual light beams, are in classical states, because they have no phase-sensitive auto-covariances. Thus their entanglement, which is a quantum feature, shows itself in their phase-sensitive cross covariance, because it exceeds the limit set by classical physics given their auto-covariance functions [18]. To enable closed-form solutions for the field-of-view, spatial resolution, and image contrast of a lensless SPDC ghost image, we shall take the preceding auto-covariance functions to be cross-spectrally pure Gaussian-Schell model forms,

$$K_{SS}^{(n)}(\boldsymbol{\rho}_1, t_1; \boldsymbol{\rho}_2, t_2) = K_{II}^{(n)}(\boldsymbol{\rho}_1, t_1; \boldsymbol{\rho}_2, t_2) = \mathcal{K}(\boldsymbol{\rho}_1, \boldsymbol{\rho}_2) \mathcal{R}(t_1 - t_2), \tag{11}$$

where the spatial and temporal terms are as given for the pseudothermal source. For the phase-sensitive cross covariance, we will assume maximally-entangled light [18,30], so that:

$$K_{SI}^{(p)}(\boldsymbol{\rho}_1, t_1; \boldsymbol{\rho}_2, t_2) = \frac{2P}{\pi a_0^2} e^{-(|\boldsymbol{\rho}_1|^2 + |\boldsymbol{\rho}_2|^2)/a_0^2} \left[i e^{-|\boldsymbol{\rho}_1 - \boldsymbol{\rho}_2|^2/2\rho_0^2} e^{-(t_1 - t_2)^2/2T_0^2} + (2/\pi)^{1/4} \sqrt{\frac{a_0^2}{PT_0\rho_0^2}} e^{-|\boldsymbol{\rho}_1 - \boldsymbol{\rho}_2|^2/\rho_0^2} e^{-(t_1 - t_2)^2/T_0^2} \right]. \tag{12}$$

Note that $\mathcal{I} \equiv PT_0\rho_0^2/a_0^2$, which is the average number of signal (or idler) photons per spatiotemporal mode, plays a key role in these SPDC statistics. Under typical cw operating conditions we have that $\mathcal{I} \ll 1$, i.e., the source has very low brightness. In this case the second term in Eq. (12) dominates the first and is also much stronger than the auto-covariance terms. As a result, if a photon pair is detected in photon-coincidence measurements made over an observation interval short enough that multiple-pair detections can be ignored, then the source’s post-selected output can be regarded as a biphoton [34] whose spatial-frequency/temporal-frequency wave function is the Fourier transform (in space and time) of the second term in Eq. (12),⁴

⁴ This state is not normalizable, i.e., $_{SI} \langle \psi | \psi \rangle_{SI} = \infty$, but it captures the entangled nature of the signal and idler.

$$\begin{aligned}
 |\psi\rangle_{SI} \propto & \int \frac{d\Omega}{2\pi} \int \frac{d\mathbf{k}_S}{(2\pi)^2} \int \frac{d\mathbf{k}_I}{(2\pi)^2} e^{-|\mathbf{k}_S - \mathbf{k}_I|^2 a_0^2/8} e^{-|\mathbf{k}_S + \mathbf{k}_I|^2 \rho_0^2/16} \\
 & \times e^{-\Omega^2 T_0^2/4} |\mathbf{k}_S, \Omega\rangle_S |-\mathbf{k}_I, -\Omega\rangle_I.
 \end{aligned}
 \tag{13}$$

In Eq. (13), \mathbf{k}_S , \mathbf{k}_I are the transverse wave vectors, Ω is the frequency detuning from the center frequency ω_0 , and $|\mathbf{k}_S, \Omega\rangle_S$, $|-\mathbf{k}_I, -\Omega\rangle_I$ denotes the single-photon states of the signal (idler), with transverse wave vector \mathbf{k}_S ($-\mathbf{k}_I$) and frequency detuning Ω ($-\Omega$).

Conversely, when $\mathcal{I} \gg 1$, as has been achieved in pulse-pumped SPDC [35], the first term in Eq. (12) dominates the second, and cross correlating photocurrent measurements on the signal and idler beams mimic those of Gaussian-state light whose phase-sensitive cross correlation is at the limit set by classical physics [30]. That said, however, 50–50 combining of such high-brightness signal and idler fields will produce highly nonclassical outputs with strong quadrature-noise squeezing. The interested reader may consult [15, 18, 30] for the performance of ghost imaging systems that use classical-state light with phase-sensitive cross correlations. In all that follows, however, we will limit our attention for phase-sensitive sources to the maximally-entangled SPDC model given above and its biphoton (low-brightness, low-flux) specialization.

2.2 Semiclassical versus quantum photodetection

Inasmuch as reconciling “quantum ”and “classical” interpretations of pseudothermal ghost imaging is a central theme of this paper, it behooves us to be absolutely clear as to what we mean by these terms. Light is intrinsically quantum mechanical, and high-sensitivity photodetection is a quantum measurement capable of revealing nonclassical features in its illumination. Therefore *all* optical imaging phenomena are fundamentally quantum mechanical. However, it has long been known [17, 36] that quantitatively identical measurement statistics result in all three basic photodetection paradigms—direct detection, homodyne detection, and heterodyne detection—when the illumination’s quantum state is a coherent state or a classically-random mixture of coherent states and the semiclassical theory of photodetection is employed, i.e., the field is treated classically and the discreteness of the electron charge in the detector leads to shot-noise generation. Thus, in all that follows we shall say that a ghost-imaging configuration is “classical” if its measurement statistics are correctly described by the use of semiclassical photodetection theory, and that the configuration is “quantum” if a correct description of its measurement statistics *requires* the use of quantum photodetection theory. In the rest of this subsection we give a very brief review of these two photodetection theories, for a more detailed review the reader should consult [17].

2.2.1 Semiclassical photodetection

Suppose that a classical field $E_z(\boldsymbol{\rho}, t)e^{-i\omega_0 t}$ illuminates a photodetector whose active region \mathcal{A} lies in the z plane. According to semiclassical photodetection theory, charge carriers—free electrons in a photomultiplier tube, hole-electron pairs in a

semiconductor photodiode—are created in a conditional Poisson-process manner in response to this illumination. When this shot noise, plus any intrinsic randomness in the classical field, dominate other sources of noise in the detector, as we shall assume throughout our analysis, the output photocurrent $i(t)$ has the following statistics. Given knowledge of the classical photon-flux,

$$P(t) \equiv \int_{\mathcal{A}} d\boldsymbol{\rho} |E_z(\boldsymbol{\rho}, t)|^2, \tag{14}$$

at all times, $i(t)/q$ is an inhomogeneous Poisson impulse train with rate function $\mu(t) \equiv \eta P(t)$. Here, q is the electron charge,⁵ $0 < \eta \leq 1$ is the detector’s quantum efficiency at wavelength $\lambda_0 = 2\pi c/\omega_0$, and we have taken the detector’s output circuit to have infinite bandwidth.⁶ Consequently, when $E_z(\boldsymbol{\rho}, t)$ is a classical random process, we have that the photocurrent’s mean and covariance function obey

$$\langle i(t) \rangle = q\eta \langle P(t) \rangle, \tag{15}$$

and

$$K_{ii}(t_1, t_2) \equiv \langle \Delta i(t) \Delta i(u) \rangle = q^2 \eta \langle P(t) \rangle \delta(t_1 - t_2) + q^2 \eta^2 K_{PP}(t_1, t_2), \tag{16}$$

respectively, where $\Delta i(t) \equiv i(t) - \langle i(t) \rangle$, and $K_{PP}(t_1, t_2)$ is the classical photon-flux’s covariance function. The first term on the right in Eq. (16) is the shot-noise contribution while the second term is due to randomness in the illuminating photon flux. When $E_z(\boldsymbol{\rho}, t)$ is a zero-mean Gaussian random process in space and time, as will be the case for the classical model of pseudothermal ghost imaging, we have that

$$\langle P(t) \rangle = \int_{\mathcal{A}} d\boldsymbol{\rho} K_{E_z E_z}^{(n)}(\boldsymbol{\rho}, t; \boldsymbol{\rho}, t), \tag{17}$$

and

$$K_{PP}(t_1, t_2) = \int_{\mathcal{A}} d\boldsymbol{\rho}_1 \int_{\mathcal{A}} d\boldsymbol{\rho}_2 \left[\left| K_{E_z E_z}^{(n)}(\boldsymbol{\rho}_1, t_1; \boldsymbol{\rho}_2, t_2) \right|^2 + \left| K_{E_z E_z}^{(p)}(\boldsymbol{\rho}_1, t_1; \boldsymbol{\rho}_2, t_2) \right|^2 \right], \tag{18}$$

in terms of the normally-ordered and phase-sensitive covariances of $E_z(\boldsymbol{\rho}, t)$.⁷

⁵ We have ignored, by assumption, any current-multiplication randomness, as occurs in photomultipliers and avalanche photodiodes. Thus, without loss of generality, we are using the electron charge as the charge released per charge-carrier generation.

⁶ This infinite-bandwidth assumption is not restrictive because explicit photocurrent filtering will be employed in the ghost-imaging calculations to follow.

⁷ Equation (18) follows from the definition of $P(t)$ and the classical moment-factoring theorem for Gaussian random processes [37].

When two classical fields $E_b(\boldsymbol{\rho}, t)e^{-i\omega_0 t}$ and $E_p(\boldsymbol{\rho}, t)e^{-i\omega_0 t}$ illuminate bucket and scanning-pinhole photodetectors, as will be the case in lensless pseudothermal ghost imaging, the shot noises in their respective photocurrents $i_b(t)$ and $i_p(t)$ will be statistically independent, but statistical dependence between any randomness in the classical photon-fluxes,

$$P_m(t) \equiv \int_{\mathcal{A}_m} d\boldsymbol{\rho} |E_m(\boldsymbol{\rho}, t)|^2, \quad \text{for } m = b, p, \tag{19}$$

will lead to a nonzero cross-covariance between these photocurrents. When the classical fields are zero-mean, jointly-Gaussian random processes, the individual photocurrents' means and auto-covariances are as given above and their cross covariance is

$$\begin{aligned} K_{i_b i_p}(t_1, t_2) &\equiv \langle \Delta i_b(t_1) \Delta i_p(t_2) \rangle = q^2 \eta^2 K_{P_b P_d}(t_1, t_2) \tag{20} \\ &= q^2 \eta^2 \int_{\mathcal{A}_b} d\boldsymbol{\rho}_1 \int_{\mathcal{A}_p} d\boldsymbol{\rho}_2 \left[\left| K_{E_b E_p}^{(n)}(\boldsymbol{\rho}_1, t_1; \boldsymbol{\rho}_2, t_2) \right|^2 \right. \\ &\quad \left. + \left| K_{E_b E_p}^{(p)}(\boldsymbol{\rho}_1, t_1; \boldsymbol{\rho}_2, t_2) \right|^2 \right]. \tag{21} \end{aligned}$$

This cross-covariance expression will provide the key to semiclassical understanding of pseudothermal ghost imaging.

2.2.2 Quantum theory of photodetection

According to the quantum theory of photodetection [17,36], the classical photocurrent $i(t)$ resulting from illumination of an active-region \mathcal{A} , quantum-efficiency η photodetector in the z plane by a photon-units positive-frequency quantum field $\hat{E}_z(\boldsymbol{\rho}, t)e^{-i\omega_0 t}$ is a random process whose classical statistics coincide with the quantum measurement statistics of the photocurrent operator $\hat{i}(t)$ that is given by

$$\hat{i}(t) = \int_{\mathcal{A}} d\boldsymbol{\rho} \hat{E}_z^\dagger(\boldsymbol{\rho}, t) \hat{E}'_z(\boldsymbol{\rho}, t). \tag{22}$$

Here, we have

$$\hat{E}'_z(\boldsymbol{\rho}, t) \equiv \sqrt{\eta} \hat{E}_z(\boldsymbol{\rho}, t) + \sqrt{1 - \eta} \hat{E}_{z_v}(\boldsymbol{\rho}, t), \tag{23}$$

where $\hat{E}_{z_v}(\boldsymbol{\rho}, t)e^{-i\omega_0 t}$ is a vacuum-state, photon-units, positive-frequency field operator whose presence contributes quantum noise to $\hat{i}(t)$ when $\eta < 1$ prevails.

If the field $\hat{E}_z(\boldsymbol{\rho}, t)$ is in the coherent state $|E_z(\boldsymbol{\rho}, t)\rangle$, then it turns out [17,36] that the measurement statistics for $\hat{i}(t)/q$ are those of an inhomogeneous Poisson impulse train with rate function

$$\mu(t) = \eta \int_{\mathcal{A}} d\boldsymbol{\rho} |E_z(\boldsymbol{\rho}, t)|^2, \tag{24}$$

i.e., they are identical to those of semiclassical theory for deterministic illumination by a classical field $E_z(\boldsymbol{\rho}, t)e^{-i\omega_0 t}$. It follows that if $\hat{E}_z(\boldsymbol{\rho}, t)$ is in a random mixture of coherent states, viz., conditioned on knowledge of a classical random process $E_z(\boldsymbol{\rho}, t)$ the quantum field state is the coherent state $|E_z(\boldsymbol{\rho}, t)\rangle$, then the statistics obtained from quantum photodetection coincide with those obtained from semiclassical photodetection of the classical, random positive-frequency field $E_z(\boldsymbol{\rho}, t)e^{-i\omega_0 t}$. This same quantum-to-semiclassical equivalence applies to the case of quantum fields, $\hat{E}_b(\boldsymbol{\rho}, t)$ and $\hat{E}_p(\boldsymbol{\rho}, t)$, illuminating bucket and scanning-pinhole photodetectors when their joint state is a coherent state or a random mixture of such states, as is the case for pseudothermal lensless ghost imaging.

In quantum photodetection theory, the mean and covariance of the photocurrent obey

$$\langle \hat{i}(t) \rangle = q\eta \int_{\mathcal{A}} d\boldsymbol{\rho} \langle \hat{E}_z^\dagger(\boldsymbol{\rho}, t) \hat{E}_z(\boldsymbol{\rho}, t) \rangle, \tag{25}$$

and⁸

$$\begin{aligned} K_{ii}^z(t_1, t_2) &= q^2\eta \int_{\mathcal{A}} d\boldsymbol{\rho} \langle \hat{E}_z^\dagger(\boldsymbol{\rho}, t_1) \hat{E}_z(\boldsymbol{\rho}, t_1) \rangle \delta(t_1 - t_2) \\ &\quad + q^2\eta^2 \int_{\mathcal{A}} d\boldsymbol{\rho}_1 \int_{\mathcal{A}} d\boldsymbol{\rho}_2 \left[\langle \hat{E}_z^\dagger(\boldsymbol{\rho}_1, t_1) \hat{E}_z^\dagger(\boldsymbol{\rho}_2, t_2) \hat{E}_z(\boldsymbol{\rho}_1, t_1) \hat{E}_z(\boldsymbol{\rho}_2, t_2) \rangle \right. \\ &\quad \left. - \langle \hat{E}_z^\dagger(\boldsymbol{\rho}_1, t_1) \hat{E}_z(\boldsymbol{\rho}_1, t_1) \rangle \langle \hat{E}_z^\dagger(\boldsymbol{\rho}_2, t_2) \hat{E}_z(\boldsymbol{\rho}_2, t_2) \rangle \right]. \end{aligned} \tag{26}$$

Although these expressions look similar to their semiclassical counterparts, there is a very significant difference in their covariances. Specifically, the second term in the semiclassical-photocurrent covariance formula from Eq. (16) is positive-semidefinite, representing the noise contributed to the photocurrent by fluctuations in the classical illumination $E_z(\boldsymbol{\rho}, t)$. On the other hand, the second term in the quantum-photocurrent covariance Eq. (26) need *not* be positive-semidefinite. Thus in quantum photodetection it is possible to have lower-than-shot-noise behavior of the photocurrent, something that is impossible in semiclassical theory.

Of interest for the ghost imaging work to follow is the specialization of the preceding mean and covariance formulas to the case of zero-mean Gaussian-state light, which may either be a classical state, as for example with pseudothermal light, or a quantum state, e.g., squeezed-state light. We have that

⁸ The delta function in Eq. (26) arises from the $[\hat{E}_z(\boldsymbol{\rho}_1, t_1), \hat{E}_z^\dagger(\boldsymbol{\rho}_2, t_2)] = \delta(\boldsymbol{\rho}_1 - \boldsymbol{\rho}_2)\delta(t_1 - t_2)$ commutator.

$$\langle \hat{i}(t) \rangle = q\eta \int_{\mathcal{A}} d\boldsymbol{\rho} K_{\hat{E}_z \hat{E}_z}^{(n)}(\boldsymbol{\rho}, t; \boldsymbol{\rho}, t), \tag{27}$$

and⁹

$$\begin{aligned} K_{\hat{i}\hat{i}}(t_1, t_2) &= q^2\eta \int_{\mathcal{A}} d\boldsymbol{\rho} K_{\hat{E}_z \hat{E}_z}^{(n)}(\boldsymbol{\rho}, t_1; \boldsymbol{\rho}, t_1)\delta(t_1 - t_2) + q^2\eta^2 \int_{\mathcal{A}} d\boldsymbol{\rho}_1 \int_{\mathcal{A}} d\boldsymbol{\rho}_2 \\ &\times \left[\left| K_{\hat{E}_z \hat{E}_z}^{(n)}(\boldsymbol{\rho}_1, t_1; \boldsymbol{\rho}_2, t_2) \right|^2 + \left| K_{\hat{E}_z \hat{E}_z}^{(p)}(\boldsymbol{\rho}_1, t_1; \boldsymbol{\rho}_2, t_2) \right|^2 \right], \end{aligned} \tag{28}$$

in terms of the quantum field’s normally-ordered and phase-sensitive covariances. These results appear identical to their semiclassical counterparts—from Eqs. (15)–(18)—but the reader is cautioned to remember that quantum fields can have stronger phase-sensitive covariances than classical physics permits.

When two zero-mean, jointly-Gaussian quantum fields illuminate bucket and scanning-pinhole photodetectors, the resulting photocurrents have means and auto-covariance functions as given in the preceding paragraph and a cross covariance that obeys

$$\begin{aligned} &K_{\hat{i}_b \hat{i}_p}(t_1, t_2) \\ &= q^2\eta^2 \int_{\mathcal{A}_b} d\boldsymbol{\rho}_1 \int_{\mathcal{A}_p} d\boldsymbol{\rho}_2 \left[\left| K_{\hat{E}_b \hat{E}_p}^{(n)}(\boldsymbol{\rho}_1, t_1; \boldsymbol{\rho}_2, t_2) \right|^2 + \left| K_{\hat{E}_b \hat{E}_p}^{(p)}(\boldsymbol{\rho}_1, t_1; \boldsymbol{\rho}_2, t_2) \right|^2 \right]. \end{aligned} \tag{29}$$

Again we have a formula apparently the same as the semiclassical case, see Eq. (21), but the reader is reminded that quantum fields admit to phase-sensitive cross-covariance functions that exceed the bounds of classical physics. As we shall see in Sect. 3, Eq. (29) will be the foundation for the field-of-view, spatial resolution, and image contrast behavior of quantum ghost imaging.

2.3 Coherence propagation for phase-insensitive and phase-sensitive light

The theory of partial coherence has a long and storied history in classical statistical optics, see, e.g., [39], with many applications in imaging and interferometry. The vast majority of this work addresses sources whose positive-frequency fields are statistically stationary in time, hence their baseband complex envelopes only have phase-insensitive covariance functions. In contrast, the quantum optics of squeezed-state generation depends on second-order nonlinear interactions that produce fields whose baseband field operators have nonzero phase-insensitive and phase-sensitive covariance functions, see, e.g., [40]. During the past decade there has

⁹ The second term in this auto-covariance follows from the quantum version of Gaussian moment-factoring [38].

been great interest in exploiting biphoton states—obtained from SPDC—in imaging systems, including ghost imaging. As a result, coherence theory for such sources has been developed [41], and its behavior compared to classical, phase-insensitive coherence theory. Here we shall quickly summarize a unified treatment of coherence theory that encompasses classical and quantum sources—in the sense of Sect. 2.2—and covers both phase-insensitive and phase-sensitive covariance functions [42]. We will restrict our attention to quasimonochromatic, paraxial, scalar fields, which will suffice for our analysis of ghost imaging. Hence the quasimonochromatic Huygens–Fresnel principle provides the necessary foundation for coherence propagation.

Given a classical quasimonochromatic, paraxial, positive-frequency scalar field $E_0(\boldsymbol{\rho}, t)e^{-i\omega_0 t}$ over the $z = 0$ plane that is propagating in the $+z$ direction, the resulting classical field $E_L(\boldsymbol{\rho}', t)$ in the $z = L$ plane is given by¹⁰

$$E_L(\boldsymbol{\rho}', t) = \int d\boldsymbol{\rho} E_0(\boldsymbol{\rho}, t - L/c)h_L(\boldsymbol{\rho}' - \boldsymbol{\rho}), \tag{30}$$

where

$$h_L(\boldsymbol{\rho}) \equiv \frac{e^{ik_0 L + ik_0 |\boldsymbol{\rho}|^2 / 2L}}{i\lambda_0 L}, \tag{31}$$

is the Huygens–Fresnel principle Green’s function (spatial impulse response), and $k_0 \equiv 2\pi/\lambda_0$ is the wave number. It turns out that the *same* quasimonochromatic Huygens–Fresnel principle governs the propagation of a quasimonochromatic, paraxial, positive-frequency scalar field operator $\hat{E}_0(\boldsymbol{\rho}, t)e^{-i\omega_0 t}$ from $z = 0$ to $z = L$, viz., all that needs to be done in Eq. (31) is to replace the classical baseband fields, $E_0(\boldsymbol{\rho}, t)$ and $E_L(\boldsymbol{\rho}', t)$, with their field-operator counterparts, $\hat{E}_0(\boldsymbol{\rho}, t)$ and $\hat{E}_L(\boldsymbol{\rho}', t)$ [17, 43].

It is well known in classical random-process theory that Gaussian random processes remain Gaussian under linear transformations. The linearity of Eq. (30) then implies that if $E_0(\boldsymbol{\rho}, t)$ is a Gaussian process, so too is $E_L(\boldsymbol{\rho}', t)$. The same closure under linear transformations applies in the quantum case to Gaussian states [17]. Hence the quantum version of Eq. (30) implies that $\hat{E}_L(\boldsymbol{\rho}', t)$ will be in a Gaussian state if $\hat{E}_0(\boldsymbol{\rho}, t)$ is in a Gaussian state.

The Gaussian states of interest for our study of ghost imaging will all have zero means, so that we only have to propagate phase-insensitive and phase-sensitive covariance functions from the input plane ($z = 0$) to the output plane ($z = L$) to obtain a complete statistical characterization of the output field, be it classical or quantum. At this point, standard linear systems theory leads to

$$K_{\hat{E}_L \hat{E}_L}^{(n)}(\boldsymbol{\rho}'_1, t_1; \boldsymbol{\rho}'_2, t_2) = \int d\boldsymbol{\rho}_1 \int d\boldsymbol{\rho}_2 K_{\hat{E}_0 \hat{E}_0}^{(n)}(\boldsymbol{\rho}_1, t_1 - L/c; \boldsymbol{\rho}_2, t_2 - L/c) \times h_L^*(\boldsymbol{\rho}'_1 - \boldsymbol{\rho}_1)h_L(\boldsymbol{\rho}'_2 - \boldsymbol{\rho}_2) \tag{32}$$

¹⁰ Equation (31) is the familiar monochromatic Huygens–Fresnel principle augmented by the direct-path propagation delay, L/c , to account for the quasimonochromatic nature of the source.

and

$$K_{\hat{E}_L \hat{E}_L}^{(p)}(\boldsymbol{\rho}'_1, t_1; \boldsymbol{\rho}'_2, t_2) = \int d\boldsymbol{\rho}_1 \int d\boldsymbol{\rho}_2 K_{\hat{E}_0 \hat{E}_0}^{(p)}(\boldsymbol{\rho}_1, t_1 - L/c; \boldsymbol{\rho}_2, t_2 - L/c) \times h_L(\boldsymbol{\rho}'_1 - \boldsymbol{\rho}_1) h_L(\boldsymbol{\rho}'_2 - \boldsymbol{\rho}_2) \tag{33}$$

for quantum-covariance propagation. Classical-covariance propagation is governed by the same equations with $K_{E_z E_z}^{(x)}$ appearing in lieu of $K_{\hat{E}_z \hat{E}_z}^{(x)}$ for $x = n, p$, and $z = 0, L$. Furthermore, a similar development applies to propagation of the (quantum or classical) cross-covariance functions between signal and reference fields, as will be needed in the Sect. 3 analysis of lensless ghost imaging.

The formal results, given in Eqs. (32) and (33), contain but do not explicitly communicate the physical differences between phase-insensitive and phase-sensitive coherence propagation. To make those differences explicit, let us examine the implications of the preceding coherence-propagation equations when

$$K_{\hat{E}_0 \hat{E}_0}^{(n)}(\boldsymbol{\rho}_1, t_1; \boldsymbol{\rho}_2, t_2) = K_{\hat{E}_0 \hat{E}_0}^{(p)}(\boldsymbol{\rho}_1, t_1; \boldsymbol{\rho}_2, t_2) = \mathcal{K}(\boldsymbol{\rho}_1, \boldsymbol{\rho}_2) \mathcal{R}(t_1 - t_2), \tag{34}$$

where \mathcal{K} and \mathcal{R} are given by Eqs. (6) and (7), respectively.¹¹ Quasimonochromatic, paraxial coherence propagation does not change the temporal portions of these covariance functions, i.e., from Eqs. (32) and (33) we find that

$$K_{\hat{E}_L \hat{E}_L}^{(x)}(\boldsymbol{\rho}'_1, t_1; \boldsymbol{\rho}'_2, t_2) = \mathcal{K}^{(x)}(\boldsymbol{\rho}'_1, \boldsymbol{\rho}'_2) \mathcal{R}(t_1 - t_2), \quad \text{for } x = n, p, \tag{35}$$

where

$$\begin{aligned} & \mathcal{K}^{(n)}(\boldsymbol{\rho}'_1, \boldsymbol{\rho}'_2) \\ &= \frac{2P}{\pi a_L^2} e^{-ik_0(|\boldsymbol{\rho}'_1|^2 - |\boldsymbol{\rho}'_2|^2)/2L - |\boldsymbol{\rho}'_1 + \boldsymbol{\rho}'_2|^2/2a_L^2 - |\boldsymbol{\rho}'_1 - \boldsymbol{\rho}'_2|^2/2\rho_L^2}, \quad \text{for } \frac{k_0 \rho_0 a_0}{2L} \ll 1, \end{aligned} \tag{36}$$

and

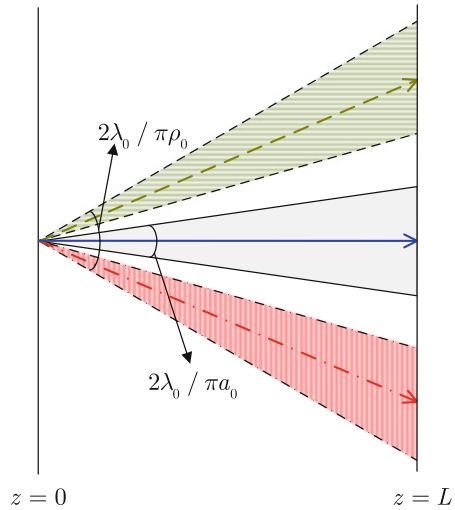
$$\begin{aligned} & \mathcal{K}^{(p)}(\boldsymbol{\rho}'_1, \boldsymbol{\rho}'_2) \\ &= \frac{2P}{\pi a_L^2} e^{ik_0(|\boldsymbol{\rho}'_1|^2 + |\boldsymbol{\rho}'_2|^2)/2L - |\boldsymbol{\rho}'_1 + \boldsymbol{\rho}'_2|^2/2\rho_L^2 - |\boldsymbol{\rho}'_1 - \boldsymbol{\rho}'_2|^2/2a_L^2}, \quad \text{for } \frac{k_0 a_0^2}{2L} \ll 1, \end{aligned} \tag{37}$$

where $a_L \equiv \lambda_0 L / \pi \rho_0$ and $\rho_L \equiv \lambda_0 L / \pi a_0$.¹² Equations (35)–(37) exhibit interesting behaviors in both their temporal and spatial dependencies, as we now explain. More details can be found in [18] and [42].

¹¹ Here we have chosen to use the classical spatial term from our SPDC $K_{SI}^{(p)}(\boldsymbol{\rho}_1, t_1, \boldsymbol{\rho}_2, t_2)$ expression. The quantum term’s propagation behavior is similar.

¹² The inequalities assumed in Eqs. (36) and (37) are far-field conditions, see below.

Fig. 5 Far-field, phase-insensitive spatial coherence behavior of the baseband field operator $\hat{E}_L(\boldsymbol{\rho}', t)$ with phase-sensitive covariance function from Eq. (36) [18]. Three plane-wave components are shown here as three arrows with different colors (and line styles). The plane waves with which they have phase-insensitive correlation lie within the shaded cones of the same color (and same line-style borders). Because phase-insensitive coherence is quasimonoplanatic, the coherence cone for each plane wave is centered on its own propagation direction (Color figure online)

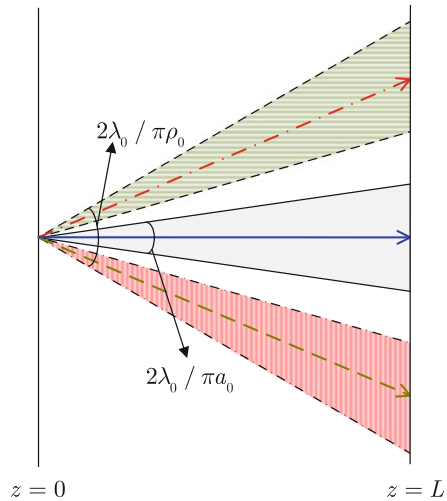


The time-stationarity of \mathcal{R} implies that phase-insensitive fluctuations at detuning Ω from the field’s center frequency ω_0 are uncorrelated with those at detuning $\Omega' \neq \Omega$, but the phase-sensitive fluctuations at detuning Ω are only correlated with those at detuning $-\Omega$ from ω_0 . The monochromatic behavior of the phase-insensitive covariance—every frequency uncorrelated with all others—is well known. The bichromatic behavior of the phase-sensitive covariance is less well known, but fully consistent with the biphoton state from Eq. (13), in which a signal photon at detuning Ω always has a companion idler photon at detuning $-\Omega$.

Equation (36) bears a striking similarity to Eq. (6). It differs in two principal ways: the presence of phase-curvature terms in the former that are absent from the latter, and the replacement of the source-plane intensity and coherence radii, a_0 and ρ_0 , with their far-field output-plane counterparts, a_L and ρ_L . Because we have assumed a low-spatial-coherence source, i.e., $\rho_0 \ll a_0$, the output plane intensity and coherence radii are the usual van Cittert–Zernike Theorem results [39]. Note that this low spatial coherence allows us to use Fraunhofer (far-field) propagation, rather than Fresnel propagation, when $k_0\rho_0 a_0/2L \ll 1$, rather than the much more restrictive far-field condition, $k_0 a_0^2/2L \ll 1$, which applies to a collimated, fully-coherent Gaussian beam of intensity-radius a_0 . As shown in Fig. 5, the phase-insensitive fluctuations are quasimonoplanatic, in that any particular plane-wave component’s phase-insensitive fluctuations are only correlated with those within a narrow cone of propagation directions centered on its own.

Like the temporal behavior of phase-insensitive fluctuations, this spatial characteristic is well known from classical coherence theory. The far-field spatial characteristics of the phase-sensitive fluctuations are rather different from the preceding phase-insensitive case. First, its far-field condition is much more stringent than that for phase-insensitive coherence, coinciding with the one for the collimated, fully-coherent Gaussian beam. Second, as shown in Fig. 6, it is quasibiplanatic, i.e., any particular plane-wave component’s phase-sensitive fluctuations are only correlated with those within a narrow cone of propagation directions centered

Fig. 6 Far-field, phase-sensitive spatial coherence behavior of the baseband field operator $\hat{E}_L(\rho', t)$ with phase-sensitive covariance function from Eq. (37) [18]. Three plane-wave components are shown here as three arrows with different colors (and line styles). The plane waves with which they have phase-sensitive correlation are shown as shaded cones having the same color (and same line-style borders). Because phase-sensitive coherence is quasibiplanatic, the coherence cone for each plane wave component is centered around its mirror image about the optical (z) axis (Color figure online)



on the mirror image about the z axis of its own. This quasibiplanatic behavior is seen in the biphoton state from Eq. (13) in that a signal photon at transverse propagation vector \mathbf{k}_S is accompanied by an idler photon at transverse propagation vector $-\mathbf{k}_I$ that satisfies $|\mathbf{k}_S - \mathbf{k}_I| \leq 2/a_0$.

3 Ghost imaging in transmission

Armed with the tools from Sect. 2, we are well prepared to address ghost-image formation for both quantum (biphoton) and classical (pseudothermal) sources. In this section we shall do so for single-wavelength operation and objects viewed in transmission. The unified Gaussian-state framework of [15] permits the field-of-view, spatial resolution, image contrast, and signal-to-noise ratio (SNR) of both cases to be derived from a common quantum-mechanical formulation. For the pseudothermal source, however, a quantitatively identical treatment results from the use of semiclassical photodetection. We shall content ourselves with a quick review of the Gaussian-state results for field-of-view, spatial resolution, and image contrast.¹³ Of greater importance, however, is the physical understanding of ghost-image formation. The Gaussian-state treatment implies that the ghost image of a transmission mask arises from the photon flux-density cross correlation between the light hitting the high-spatial-resolution detector and the light that has passed through the transmission mask and illuminates the bucket detector. Moreover, for pseudothermal ghost imaging analyzed with semiclassical photodetection theory, this photon-flux density cross correlation is the intensity cross-correlation of the classical fields. On the other hand, ghost imaging with an SPDC source has a natural interpretation as two-photon interference. Furthermore, the mathematics for the semiclassical treatment of pseudothermal ghost imaging can be rearranged to admit

¹³ The reader is directed to [18,30,31] for SNR behavior, which will not be discussed here.

to a similar interference interpretation. Thus we will devote Sect. 4 to the development and discussion of these alternative interpretations of ghost-image formation.

3.1 SPDC ghost imaging

Figure 7 shows the configuration we will consider for quantum-source ghost imaging in transmission. Here the signal and idler from a frequency-degenerate spontaneous parametric downconverter provide, respectively, the signal, $\hat{E}_S(\boldsymbol{\rho}, t)$, and reference, $\hat{E}_R(\boldsymbol{\rho}, t)$, for lensless ghost imaging of a transmission mask of field-transmission function $T(\boldsymbol{\rho})$ located L m away from the source. The ghost image is formed by cross correlating the photocurrents, $i_b(t)$ and $i_p(t)$, from the bucket and scanning-pinhole detectors. We will assume that the signal and idler from the downconverter are in the zero-mean, jointly-Gaussian state specified by the Gaussian-Schell model covariances from Sect. 2.1, that L m of free space propagation takes these fields into the far field, as discussed in Sect. 2.3, and that the photodetectors are characterized by quantum photodetection theory, as described in Sect. 2.2, with the addition of the DC-coupled output filter $H_B(\Omega) = e^{-2\Omega^2/\Omega_B^2}$ with unity DC response and bandwidth Ω_B . The output of this correlator, when the pinhole location is $\boldsymbol{\rho}_p$, is the ghost image at that point. The full image is thus built up by scanning the pinhole over the region illuminated by the reference light. Note that the low-flux limit of the photocurrent cross correlation shown in this figure is equivalent to the photon coincidence-counting that is typically employed in SPDC ghost-imaging experiments.

To understand the field-of-view, spatial resolution, and image contrast afforded by the Fig. 7 configuration it suffices to compute the ensemble-average image $\langle C(\boldsymbol{\rho}_p) \rangle$, because it is indicative of what will be obtained experimentally from long-duration time averaging. Because the baseband field operators for our SPDC source have covariances that are statistically stationary in time, we have that

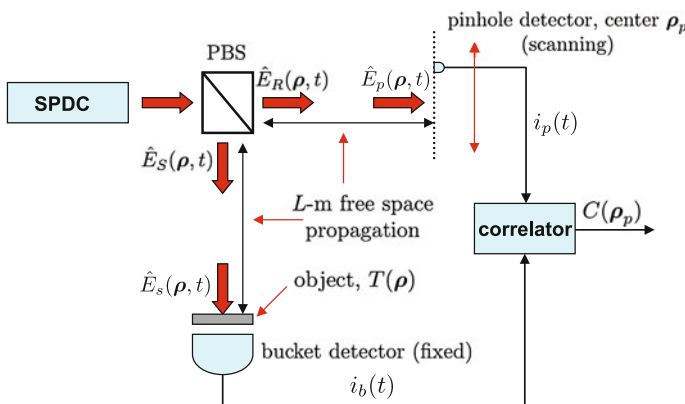


Fig. 7 Configuration for lensless ghost imaging of a transmission mask using an SPDC source. Not shown is $\hat{E}_b(\boldsymbol{\rho}, t) = T(\boldsymbol{\rho})\hat{E}_s(\boldsymbol{\rho}, t) + \sqrt{1 - |T(\boldsymbol{\rho})|^2}\hat{E}_{sv}(\boldsymbol{\rho}, t)$, the quantum field that illuminates the bucket detector, where $\hat{E}_{sv}(\boldsymbol{\rho}, t)$ is a vacuum-state field operator needed to preserve commutator brackets in the presence of transmission loss through the mask $T(\boldsymbol{\rho})$

$$\langle C(\boldsymbol{\rho}_p) \rangle = \langle i_b(t) i_p(t) \rangle. \tag{38}$$

Using the photocurrent mean and cross-covariance expressions from quantum photo-detection of Gaussian-state light and accounting for the presence of the transmission mask $T(\boldsymbol{\rho})$, we then find that [15]

$$\begin{aligned} \langle C(\boldsymbol{\rho}_p) \rangle &= q^2 \eta^2 \int_{\mathcal{A}_b} d\boldsymbol{\rho} K_{\hat{E}_s \hat{E}_s}^{(n)}(\boldsymbol{\rho}, t; \boldsymbol{\rho}, t) |T(\boldsymbol{\rho})|^2 \int_{\mathcal{A}_p} d\boldsymbol{\rho} K_{\hat{E}_p \hat{E}_p}^{(n)}(\boldsymbol{\rho}, t; \boldsymbol{\rho}, t) \\ &+ q^2 \eta^2 \int d\tau_1 \int d\tau_2 \int_{\mathcal{A}_b} d\boldsymbol{\rho}_1 \int_{\mathcal{A}_p} d\boldsymbol{\rho}_2 h_B(t - \tau_1) h_B(t - \tau_2) \\ &\times |K_{\hat{E}_s \hat{E}_p}^{(p)}(\boldsymbol{\rho}_1, \tau_1; \boldsymbol{\rho}_2, \tau_2)|^2 |T(\boldsymbol{\rho}_1)|^2, \end{aligned} \tag{39}$$

where $h_B(t)$ is the impulse response associated with $H_B(\Omega)$ and \mathcal{A}_b (\mathcal{A}_p) is the bucket (pinhole) detector’s photosensitive region.

To draw out the imaging characteristics implicit in this expression let us make the following additional assumptions, which are realistic for SPDC ghost imaging: (1) the brightness of the SPDC source is sufficiently low that we can omit the first term on the right in Eq. (12) in its phase-sensitive cross covariance;¹⁴ (2) the area A_p of the pinhole detector’s sensitive region \mathcal{A}_p is small enough that the covariance functions can be taken to be constant over that region; and (3) the coherence time T_0 of the SPDC source is much less than the reciprocal bandwidth $1/\Omega_B$ of the detectors’ output filters. Under these conditions, Eq. (39) reduces to

$$\begin{aligned} \langle C(\boldsymbol{\rho}_p) \rangle &= q^2 \eta^2 A_p \left(\frac{2P}{\pi a_L^2} \right)^2 \left[e^{-2|\boldsymbol{\rho}_p|^2/a_L^2} \int_{\mathcal{A}_b} d\boldsymbol{\rho} e^{-2|\boldsymbol{\rho}|^2/a_L^2} |T(\boldsymbol{\rho})|^2 \right. \\ &\left. + \frac{\Omega_B a_0^2}{16\sqrt{\pi} P \rho_0^2} e^{-|\boldsymbol{\rho}_p|^2/a_L^2} \int_{\mathcal{A}_b} d\boldsymbol{\rho} e^{-|\boldsymbol{\rho} - \boldsymbol{\rho}_p|^2/\rho_L^2} e^{-|\boldsymbol{\rho}|^2/a_L^2} |T(-\boldsymbol{\rho})|^2 \right]. \end{aligned} \tag{40}$$

From this equation it is easy to discern the key characteristics of the low-brightness SPDC ghost image. Its field of view—measured in transverse coordinates—is $\sim\sqrt{2}a_L$ in extent, i.e., it is set by the source’s intensity radius at the transmission mask. Let us assume that $|T(\boldsymbol{\rho})|$ is nonzero only for $|\boldsymbol{\rho}| \ll a_L$, so that Eq. (40) simplifies to

¹⁴ As noted in Sect. 2.1, this is the regime wherein the Gaussian-state treatment of SPDC reduces to the post-selected biphoton approximation.

$$\langle C(\boldsymbol{\rho}_p) \rangle = q^2 \eta^2 A_p \left(\frac{2P}{\pi a_L^2} \right)^2 \left[\int_{\mathcal{A}_b} d\boldsymbol{\rho} |T(\boldsymbol{\rho})|^2 + \frac{\Omega_B a_0^2}{16\sqrt{\pi} P \rho_0^2} \int_{\mathcal{A}_b} d\boldsymbol{\rho} e^{-|\boldsymbol{\rho} - \boldsymbol{\rho}_p|^2 / \rho_L^2} |T(-\boldsymbol{\rho})|^2 \right]. \quad (41)$$

Here we see that the DC-coupled photocurrent cross correlation is comprised of a featureless background term—the first term on the right in Eq. (41)—plus an inverted image of the transmission mask’s intensity-transmission function $|T(\boldsymbol{\rho})|^2$ that has been subjected to convolution with a Gaussian point-spread function of spatial resolution ρ_L , viz., the SPDC source’s coherence radius at the transmission mask. The image contrast, taken to be the maximum of the image term in Eq. (41) divided by the background term, is approximately $\Omega_B a_L^2 / P A_T \gg 1$, for a spatially-resolved binary (one-zero) mask with area $A_T \equiv \int d\boldsymbol{\rho} |T(\boldsymbol{\rho})|^2$. The inequality applies in the low-flux (biphoton) regime, wherein at most one signal-idler pair occurs within the detectors’ $1/\Omega_B$ output-filter integration time. A derivation of the SPDC lensless ghost image that starts from the biphoton state, Eq. (13), leads to a prediction that there is *no* featureless background term [44]. Indeed SPDC ghost imaging experiments—done in the biphoton regime using photon-coincidence counting—generally have negligible background [1]. The absence of a background term, in the biphoton theory of SPDC ghost imaging, comes from that state’s being a perturbative approximation to the true Gaussian state, which omits the multiple-pair contributions responsible for the background [34].¹⁵

3.2 Pseudothermal ghost imaging

The Gaussian-state analysis of pseudothermal ghost imaging closely parallels what we have just done for the SPDC case. Figure 8 shows the configuration we shall consider for classical-source ghost imaging in transmission. Here, signal and reference fields are obtained by passing a cw laser beam through a rotating ground-glass diffuser followed by a 50–50 beam splitter. Both fields propagate over L -m-long free-space paths, after which the signal beam passes through the transmission mask $T(\boldsymbol{\rho})$ and on to a bucket detector, while the reference beam illuminates a scanning-pinhole detector. As in the previous subsection, the ghost image is formed by cross correlating the photocurrents from the bucket and scanning-pinhole detectors. Because pseudothermal light, treated quantum mechanically, is a Gaussian random mixture of coherent states, we know that the quantum photodetection treatment of the Fig. 8 setup will lead to the same statistics for the photocurrent cross correlation as found from semiclassical theory—cf. [15], which uses quantum theory, and [16], which uses semiclassical theory—and hence

¹⁵ Experimentalists lump these multiple-pair contributions into what they report as “accidental” coincidences, a category that also includes coincidences arising from dark counts and other experimental non-idealities which we are not including in this paper.

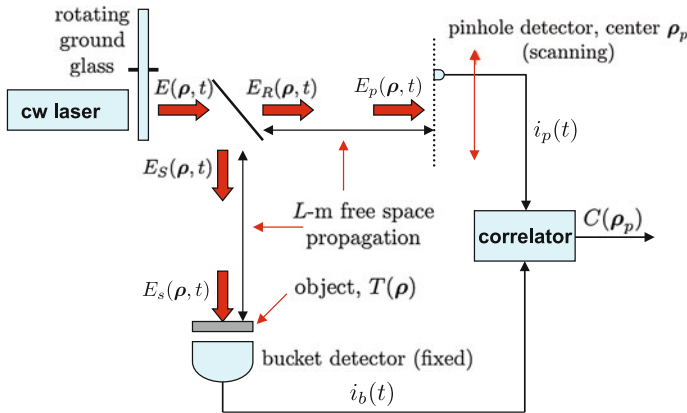


Fig. 8 Configuration for lensless ghost imaging of a transmission mask using a pseudothermal source. Not shown is $E_b(\rho, t) = T(\rho)E_s(\rho, t)$, the classical field that illuminates the bucket detector

arrive at identical results for the behavior of lensless pseudothermal ghost imaging. Therefore we have shown classical fields in Fig. 8, and we will use semiclassical analysis in what follows.

Our goal in this subsection is to determine the field-of-view, spatial resolution, and image contrast of the pseudothermal ghost image by deriving the correlator’s ensemble-average output, $\langle C(\rho_p) \rangle$. The classical signal and reference fields will be taken to be completely-correlated, zero-mean, jointly Gaussian random processes characterized by their non-zero covariances, namely

$$\begin{aligned}
 K_{E_S E_S}^{(n)}(\rho_1, t_1, \rho_2, t_2) &= K_{E_R E_R}^{(n)}(\rho_1, t_1, \rho_2, t_2) = K_{E_S E_R}^{(n)}(\rho_1, t_1, \rho_2, t_2) \\
 &= \mathcal{K}(\rho_1, \rho_2) \mathcal{R}(t_1 - t_2) = \frac{2P}{\pi a_0^2} e^{-(|\rho_1|^2 + |\rho_2|^2)/a_0^2 - |\rho_1 - \rho_2|^2/2\rho_0^2} e^{-(t_1 - t_2)^2/2T_0^2}. \quad (42)
 \end{aligned}$$

Using the photocurrent mean and cross-covariance expressions from semiclassical photodetection of Gaussian-state light and accounting for the presence of the transmission mask $T(\rho)$, we get [16]

$$\begin{aligned}
 \langle C(\rho_p) \rangle &= q^2 \eta^2 \int_{\mathcal{A}_b} d\rho K_{E_S E_S}^{(n)}(\rho, t; \rho, t) |T(\rho)|^2 \int_{\mathcal{A}_p} d\rho K_{E_p E_p}^{(n)}(\rho, t; \rho, t) \\
 &\quad + q^2 \eta^2 \int d\tau_1 \int d\tau_2 \int_{\mathcal{A}_b} d\rho_1 \int_{\mathcal{A}_p} d\rho_2 h_B(t - \tau_1) h_B(t - \tau_2) \\
 &\quad \times |K_{E_S E_p}^{(n)}(\rho_1, \tau_1; \rho_2, \tau_2)|^2 |T(\rho_1)|^2. \quad (43)
 \end{aligned}$$

To make the imaging characteristics embedded in Eq. (43) explicit, we again assume that far-field propagation has occurred and that the covariance functions are constant

over the pinhole detector’s sensitive region. Unlike the SPDC case, however, we assume that the coherence time T_0 of the pseudothermal source greatly exceeds the reciprocal bandwidth $1/\Omega_B$ of the detectors’ output filter. Under these conditions, Eq. (43) becomes

$$\begin{aligned} \langle C(\boldsymbol{\rho}_p) \rangle = & q^2 \eta^2 A_p \left(\frac{2P}{\pi a_L^2} \right)^2 e^{-2|\boldsymbol{\rho}_p|^2/a_L^2} \left[\int_{\mathcal{A}_b} d\boldsymbol{\rho} e^{-2|\boldsymbol{\rho}|^2/a_L^2} |T(\boldsymbol{\rho})|^2 \right. \\ & \left. + \int_{\mathcal{A}_b} d\boldsymbol{\rho} e^{-|\boldsymbol{\rho}-\boldsymbol{\rho}_p|^2/\rho_L^2} e^{-2|\boldsymbol{\rho}|^2/a_L^2} |T(\boldsymbol{\rho})|^2 \right]. \end{aligned} \tag{44}$$

Here we see that the field-of-view, in transverse coordinates, is $\sim a_L$, i.e., narrower than that for SPDC ghost imaging. Making the assumption that $|T(\boldsymbol{\rho})|$ is nonzero only for $|\boldsymbol{\rho}| \ll a_L$ gives us

$$\langle C(\boldsymbol{\rho}_p) \rangle = q^2 \eta^2 A_p \left(\frac{2P}{\pi a_L^2} \right)^2 \left[\int_{\mathcal{A}_b} d\boldsymbol{\rho} |T(\boldsymbol{\rho})|^2 + \int_{\mathcal{A}_b} d\boldsymbol{\rho} e^{-|\boldsymbol{\rho}-\boldsymbol{\rho}_p|^2/\rho_L^2} |T(\boldsymbol{\rho})|^2 \right]. \tag{45}$$

It is interesting to compare Eq. (45) with Eq. (41). Both consist of the same featureless background term plus a ghost-image term. The SPDC ghost image is inverted, but the pseudothermal ghost image is erect. Both ghost images have resolutions limited to ρ_L , by convolution with a Gaussian point-spread function. For a spatially-resolved binary transmission mask, the low-flux SPDC ghost image has very high contrast, whereas the image contrast of the pseudothermal ghost image is $\sim \pi \rho_L^2/A_T \ll 1$. Note, however, that the background term can be suppressed by AC coupling the detectors into the correlator, i.e., by measuring the photocurrents’ cross covariance, rather than their cross correlation, as has been done experimentally in [14]. As explained in [30], the presence of a strong background term in the pseudothermal configuration has consequences for its signal-to-noise ratio, even when AC coupling is used to eliminate its contribution to $\langle C(\boldsymbol{\rho}_p) \rangle$, i.e., the average image.

There is one final note worth making in conjunction with our Gaussian-state analysis of lensless ghost imaging. In both Figs. 7 and 8 we assumed that the source-to-detector path lengths for the signal and reference paths were the same. This is not an accidental choice. Lensless ghost imaging is *not* shadow casting. In particular, changing either path length by ΔL changes ρ_L in the ghost-imaging point-spread functions for SPDC and pseudothermal operation to $\rho_L \sqrt{1 + (\Delta L/k_0 \rho_L^2)^2}$ [16], leading to a focal region satisfying $|\Delta L|/L = 4L/k_0 a_0^2 \ll 1$ as reported for the experiments in [19].

4 Two interpretations for ghost-image formation

The Gaussian-state analysis we have presented for lensless ghost imaging in transmission is pleasing for its unified coverage of SPDC and pseudothermal operation, and for its closed-form results for the field-of-view, spatial resolution, and image contrast. It does not, however, convey sufficient intuitive understanding of ghost-image formation. Thus in this section we shall strive to develop that understanding by describing two physical interpretations that offer different insights into this image-formation process: photon-flux-density speckle correlations, and two-photon interference.

4.1 Ghost-image formation via speckle correlations

The correlator output in the lensless ghost-imaging setup shown in Fig. 7 for SPDC illumination, and in Fig. 8 for pseudothermal illumination, is the T_I -s-long time average of $i_b(t)i_p(t)$, the product of their bucket and scanning-pinhole detectors' photocurrents. For an intuitive understanding of how the ghost image arises, let us first consider the bucket and scanning-pinhole detectors' photocurrents individually. For *both* our SPDC and our pseudothermal source models, the quantum fields $\hat{E}_s(\boldsymbol{\rho}, t)$ and $\hat{E}_p(\boldsymbol{\rho}, t)$ that illuminate the transmission mask and the scanning pinhole have reduced density operators that are zero-mean Gaussian states with phase-insensitive covariances given by

$$K_{\hat{E}_m \hat{E}_m}^{(n)}(\boldsymbol{\rho}_1, t_1; \boldsymbol{\rho}_2, t_2) = \frac{2P}{\pi a_L^2} e^{-ik_0(|\boldsymbol{\rho}_1|^2 - |\boldsymbol{\rho}_2|^2)/2L - |\boldsymbol{\rho}_1 + \boldsymbol{\rho}_2|^2/2a_L^2 - |\boldsymbol{\rho}_1 - \boldsymbol{\rho}_2|^2/2\rho_L^2} \times e^{-(t_1 - t_2)^2/2T_0^2}, \quad \text{for } m = s, p, \tag{46}$$

in the far field, and no phase-sensitive covariance. Hence these reduced density operators are *classical* states, so that their individual photocurrents have statistics which are accurately characterized by semiclassical photodetection theory. Accordingly, we can regard $i_b(t)/q$ and $i_p(t)/q$ as conditional Poisson impulse trains that are driven by the classical-photon-flux densities¹⁶

$$P_b(t) \equiv \eta \int_{\mathcal{A}_b} d\boldsymbol{\rho} I_s(\boldsymbol{\rho}, t) |T(\boldsymbol{\rho})|^2, \tag{47}$$

¹⁶ For simplicity, in this section, we will assume the photodetectors have infinite electrical (output) bandwidth. This poses no problem for the pseudothermal source, as its bandwidth can easily be kept much lower than the photodetectors' electrical bandwidth. Such is not the case for the SPDC source, whose ~THz bandwidth outstrips the electrical bandwidth of available photodetectors. However, because our goal in this section is to understand the spatial characteristics of ghost-image formation, no loss of generality in treating the SPDC case ensues from our infinite-bandwidth assumption.

and

$$P_p(t) \equiv \eta \int_{\mathcal{A}_p} d\boldsymbol{\rho} I_p(\boldsymbol{\rho}, t) \approx \eta A_p I_p(\boldsymbol{\rho}_p, t), \tag{48}$$

where $\{I_m(\boldsymbol{\rho}, t) \equiv |E_m(\boldsymbol{\rho}, t)|^2 : m = s, p\}$, are the classical photon-flux densities (intensities in units of photons/m²-s) of identically-distributed, classical, zero-mean, Gaussian random processes, $\{E_m(\boldsymbol{\rho}, t) : m = s, p\}$, with phase-insensitive covariances given by Eq. (46) and no phase-sensitive covariance. It has long been known that such classical photon-flux densities consist of time-varying speckle patterns [45]. When sampled at a single space-time point, $I_m(\boldsymbol{\rho}, t)$ is an exponentially-distributed random variable. As a random process in space and time, $I_m(\boldsymbol{\rho}, t)$ has coherence time T_0 and coherence area $\pi\rho_L^2$. Were the joint state of $\hat{E}_s(\boldsymbol{\rho}, t)$ and $\hat{E}_p(\boldsymbol{\rho}, t)$ a classical state, then the joint statistics of $i_b(t)$ and $i_p(t)$ would admit to a semiclassical characterization that is identical to that derived from quantum photodetection theory. We could then say that

$$\begin{aligned} \langle C(\boldsymbol{\rho}_p) \rangle &= \left\langle \frac{1}{T_I} \int_{-T_I/2}^{T_I/2} dt i_b(t) i_p(t) \right\rangle \\ &= q^2 \eta^2 A_p \frac{1}{T_I} \int_{-T_I/2}^{T_I/2} dt \int_{\mathcal{A}_b} d\boldsymbol{\rho} \langle I_s(\boldsymbol{\rho}, t) I_p(\boldsymbol{\rho}_p, t) \rangle |T(\boldsymbol{\rho})|^2, \end{aligned} \tag{49}$$

demonstrating that the average ghost image at pinhole coordinate $\boldsymbol{\rho}_p$ is due to the average cross-correlation between the two classical speckle patterns, $I_s(\boldsymbol{\rho}, t)$ and $I_p(\boldsymbol{\rho}_p, t)$. But pseudothermal ghost imaging does obey the preceding premise: the joint state of the quantum fields $\hat{E}_s(\boldsymbol{\rho}, t)$ and $\hat{E}_p(\boldsymbol{\rho}, t)$ is classical, hence it is entirely fair to interpret the pseudothermal ghost image as arising from speckle correlations, i.e., the correlation between the photon-flux-density illumination patterns. Furthermore, it is easy to see that with pseudothermal light $I_s(\boldsymbol{\rho}, t)$ and $I_p(\boldsymbol{\rho}, t)$ have completely-correlated speckle patterns, because in the pseudothermal setup identical classical signal and reference fields exit the 50–50 beam splitter, and that complete correlation remains after each has propagated over an L -m-long free space path.

The speckle-correlation interpretation of pseudothermal ghost-image formation immediately connects to the Gaussian-state results we presented in Sect. 3.2. In particular, writing

$$\langle I_s(\boldsymbol{\rho}, t) I_p(\boldsymbol{\rho}_p, t) \rangle = \langle I_s(\boldsymbol{\rho}, t) \rangle \langle I_p(\boldsymbol{\rho}_p, t) \rangle + \langle \Delta I_s(\boldsymbol{\rho}, t) \Delta I_p(\boldsymbol{\rho}_p, t) \rangle, \tag{50}$$

leads to the first term creating the featureless background, and the second term producing the ghost image. Moreover, the $a_L = \lambda_0 L / \rho_0$ radii of the overall $\{I_m(\boldsymbol{\rho}, t)\}$ speckle patterns and their $\rho_L = \lambda_0 L / a_0$ coherence radii explain the field-of-view and spatial resolution that we found in Sect. 3.2, and the classical limit on the strength

of two fields' phase-insensitive cross covariance can be shown to imply the image contrast that was determined in that section.

The compelling nature of the photon-flux-density speckle correlation interpretation of pseudothermal ghost-image formation begs us to examine whether or not this classical interpretation has a quantum extension that encompasses SPDC ghost-image formation. It turns out that it does. Quantum photodetection theory tells us that

$$\begin{aligned} \langle C(\boldsymbol{\rho}_p) \rangle &= \left\langle \frac{1}{T_I} \int_{-T_I/2}^{T_I/2} dt \hat{i}_b(t) \hat{i}_p(t) \right\rangle \\ &= q^2 A_p \frac{1}{T_I} \int_{-T_I/2}^{T_I/2} dt \int_{\mathcal{A}_b} d\boldsymbol{\rho} \langle \hat{I}'_b(\boldsymbol{\rho}, t) \hat{I}'_p(\boldsymbol{\rho}_p, t) \rangle, \end{aligned} \tag{51}$$

where

$$\hat{I}'_m(\boldsymbol{\rho}, t) \equiv \hat{E}_m^{\dagger}(\boldsymbol{\rho}, t) \hat{E}'_m(\boldsymbol{\rho}, t), \quad \text{for } m = b, p \tag{52}$$

give the effective photon-flux-density operators. Here, we have that

$$\hat{E}'_m(\boldsymbol{\rho}, t) \equiv \sqrt{\eta} \hat{E}_m(\boldsymbol{\rho}, t) + \sqrt{1 - \eta} \hat{E}_{m_v}(\boldsymbol{\rho}, t), \quad \text{for } m = b, p, \tag{53}$$

with $\{ \hat{E}_{m_v}(\boldsymbol{\rho}, t) : m = b, p \}$ being vacuum-state field operators that contribute quantum noise when $\eta < 1$. Also, the field operator illuminating the bucket detector is found from

$$\hat{E}_b(\boldsymbol{\rho}, t) \equiv T(\boldsymbol{\rho}) \hat{E}_s(\boldsymbol{\rho}, t) + \sqrt{1 - |T(\boldsymbol{\rho})|^2} \hat{E}_{s_v}(\boldsymbol{\rho}, t), \tag{54}$$

where $\hat{E}_{s_v}(\boldsymbol{\rho}, t)$ is another vacuum-state field operator, this one accounting for propagation loss through the transmission mask $T(\boldsymbol{\rho})$. When Eq. (51) is evaluated for pseudothermal light, it reduces to the semiclassical result presented above, but what happens when Eq. (51) is evaluated for SPDC light?

For SPDC light we must stick with the quantum formulation because the joint state of $\hat{E}_b(\boldsymbol{\rho}, t)$ and $\hat{E}_p(\boldsymbol{\rho}, t)$ is nonclassical. Nevertheless, we can still expand the integrand in Eq. (51) in terms of mean values and covariance:

$$\langle \hat{I}'_b(\boldsymbol{\rho}, t) \hat{I}'_p(\boldsymbol{\rho}_p, t) \rangle = \langle \hat{I}'_b(\boldsymbol{\rho}, t) \rangle \langle \hat{I}'_p(\boldsymbol{\rho}_p, t) \rangle + \langle \Delta \hat{I}'_b(\boldsymbol{\rho}, t) \Delta \hat{I}'_p(\boldsymbol{\rho}_p, t) \rangle. \tag{55}$$

When the terms on the right are evaluated—using our Gaussian-state model for SPDC light—they of course lead to the results of Sect. 3.1 after substitution into Eq. (51). The first term in Eq. (55) creates the featureless background, while the second term is responsible for the ghost image. Furthermore, the background term—which can be evaluated from semiclassical theory, because it only depends on the reduced density

operators of the signal and idler fields—is *identical* to that of pseudothermal illumination with the same photon flux, intensity radius and coherence radius. The quantum nature of SPDC light manifests itself in the covariance term of Eq. (55), because, as we have already seen, that ghost-image term exceeds the covariance bounds set by classical physics, making the DC-coupled SPDC image one of very high contrast. So, because the individual photon-flux densities produced by SPDC light at the detectors are classical speckle patterns, and because their covariance—albeit one requiring quantum photodetection to account for its strength—yields the ghost image, it is appropriate to regard the SPDC ghost image as coming from speckle correlations, but these speckle correlations have nonclassical strength.

4.2 Ghost-image formation as two-photon interference

In Sect. 1 we alluded to the controversy that has swirled around the pseudothermal ghost image’s physical interpretation. Must it be explained quantum mechanically, or can it be regarded as arising from correlations between the intensity fluctuations in the light beams that illuminate the bucket and pinhole detectors? We have just seen that the pseudothermal ghost image *does* have a physical interpretation as arising from speckle correlations between the two detectors’ illuminations, because that interpretation accompanies the semiclassical Gaussian-state analysis of pseudothermal ghost imaging which is quantitatively identical to its quantum treatment. We went further, in Sect. 4.1, by asserting that there is a similar *quantum* speckle-correlation interpretation that applies to SPDC ghost imaging, with the principal quantum feature being that image’s having DC-coupled contrast far in excess of what classical physics allows. Now it is time to argue for SPDC ghost imaging’s having an interpretation as two-photon interference, and to see how that *quantum* interpretation has an extension to the pseudothermal case.

Let us start by considering the SPDC setup from Fig. 7 when the source is assumed to operate in the low-brightness, low-flux regime wherein we can regard its post-selected output as a biphoton.¹⁷ Using the position and time representation, instead of the wave-vector and frequency representation from Eq. (13), we can say that

$$|\psi\rangle_{SR} \propto \int dt_S \int dt_I \int d\rho_S \int d\rho_R \psi_{SR}(\rho_S, t_S; \rho_R, t_R) |\rho_S, t_S\rangle_S |\rho_R, t_R\rangle_R, \quad (56)$$

is the biphoton state of the signal and reference fields, $\hat{E}_S(\rho, t)$ and $\hat{E}_R(\rho, t)$, where

$$\psi_{SR}(\rho_S, t_S; \rho_R, t_R) = e^{-(|\rho_S|^2 + |\rho_R|^2)/a_0^2} e^{-|\rho_S - \rho_R|^2/\rho_0^2} e^{-(t_S - t_R)^2/T_0^2}, \quad (57)$$

¹⁷ The two-photon interference interpretation for SPDC ghost imaging arises from the biphoton expression for the average photon-coincidence rate between the bucket and scanning pinhole detectors—derived below—which is proportional to the point-spread-function degraded version of the object’s intensity transmission $|T(\rho)|^2$. As such, all the biphotons that contribute to the ghost image are post-selected biphotons. For the sake of brevity, however, we shall just refer to them as biphotons.

is its biphoton wave function, and $|\rho_S, t_S\rangle_S (|\rho_R, t_R\rangle_R)$ is the single-photon state of the signal (reference) at position ρ_S (ρ_R) and time t_S (t_R). Free-space propagation of the signal and reference fields over L -m-long far-field paths and passage of the former through the transmission mask lead to quantum fields $\hat{E}_b(\rho, t)$ and $\hat{E}_p(\rho_p, t)$ that impinge on the bucket and scanning-pinhole detector, respectively, which are in the biphoton state $|\psi\rangle_{bp}$ with wave function [41]

$$\begin{aligned} \psi_{bp}(\rho_b, t_b; \rho_p, t_p) &\propto T(\rho_b) \int d\rho_S \int d\rho_R h_L(\rho_b - \rho_S) h_L(\rho_p - \rho_R) \\ &\times \psi_{SR}(\rho_S, t_b - L/c; \rho_R, t_p - L/c). \end{aligned} \tag{58}$$

Continuing with our simplifying assumption of infinite electrical-bandwidth photodetectors, we have that the probability that photons will be detected simultaneously at ρ_b on the bucket detector and ρ_p on the scanning-pinhole detector at time t is proportional to the second-order Glauber coherence function [46]

$$G_{bp}^{(2)}(\rho_b, t; \rho_p, t) \equiv {}_{bp}\langle \psi | \hat{E}_b^\dagger(\rho_b, t) \hat{E}_p^\dagger(\rho_p, t) \hat{E}_b(\rho_b, t) \hat{E}_p(\rho_p, t) | \psi \rangle_{bp} \tag{59}$$

$$= |\psi_{bp}(\rho_b, t; \rho_p, t)|^2 \tag{60}$$

$$\propto |T(\rho_b)|^2 e^{-(|\rho_b|^2 + |\rho_p|^2)/a_L^2} e^{-|\rho_b + \rho_p|^2/\rho_L^2}. \tag{61}$$

In biphoton theory, the average ghost image is given by

$$\langle C(\rho_p) \rangle \propto \int_{\mathcal{A}_b} d\rho_b G_{bp}^{(2)}(\rho_b, t; \rho_p, t), \tag{62}$$

which becomes

$$\langle C(\rho_p) \rangle \propto \int_{\mathcal{A}_b} d\rho e^{-|\rho - \rho_p|^2/\rho_L^2} |T(-\rho)|^2, \tag{63}$$

when $|T(\rho)|$ is only nonzero for $|\rho| \ll a_L$.

Equation (63) shows that biphoton theory predicts a background-free SPDC ghost image whose spatial resolution is the same as what we found from Gaussian-state analysis. From this result we can also see why it was initially thought that entanglement was essential to ghost imaging. In particular, were $\hat{E}_S(\rho, t)$ and $\hat{E}_R(\rho, t)$ to be in a product state, then $\hat{E}_b(\rho, t)$ and $\hat{E}_p(\rho, t)$ would be too. The second-order Glauber coherence function of $\hat{E}_b(\rho, t)$ and $\hat{E}_p(\rho, t)$ would then factor into the product of first-order coherence functions for the individual fields, so that when the second-order function is integrated over the bucket detector, all image information about $|T(\rho)|^2$ would be lost. Of course, the reduced density operators for $\hat{E}_b(\rho, t)$ and $\hat{E}_p(\rho, t)$, when their joint state is the biphoton whose wave function is given by Eq. (58), are mixed states, each of which spreads its photon-detection probability density over a

spatial region of radius a_L that is much greater than the SPDC ghost image’s ρ_L spatial resolution. The biphoton entanglement that produces the ghost image described by Eq. (63) can then be rightly termed as originating from nonlocal two-photon interference, in which observation of a photon on the scanning-pinhole detector at location ρ_p collapses the reduced state of $\hat{E}_s(\rho, t)$ so that its photon will be detected within a ρ_L radius of location $-\rho_p$ on the transmission mask.

Having exhibited a two-photon interference interpretation for the SPDC ghost image, let us conclude this section by showing how such an interpretation can be developed for the pseudothermal ghost image. We will do so means of Eq. (62)—i.e., by assuming that the pseudothermal source is operated at very low photon flux, so that the photocurrent cross correlation in Fig. 8 can be taken to be photon-coincidence counting—in which we will use the classical, Gaussian-state expression

$$G_{bp}^{(2)}(\rho_b, t; \rho_p, t) \equiv \langle E_b^*(\rho_b, t) E_p^*(\rho_p, t) E_b(\rho_b, t) E_p(\rho_p, t) \rangle \tag{64}$$

for the second-order coherence function. From Sec. 2.3 we know that the classical fields in this coherence function are related to the output from the pseudothermal source by the quasimonochromatic Huygens–Fresnel principle,

$$E_b(\rho_b, t) = T(\rho_b) \int d\rho E(\rho, t - L/c) h_L(\rho_b - \rho), \tag{65}$$

and

$$E_p(\rho_p, t) = \int d\rho E(\rho, t - L/c) h_L(\rho_p - \rho), \tag{66}$$

where we have used $E(\rho, t) \equiv E_S(\rho, t) = E_R(\rho, t)$, which applies at the output of the 50–50 beam splitter in Fig. 8. To get at the two-photon interference interpretation we are seeking, we shall exploit the low spatial coherence of the pseudothermal source to decompose $E(\rho, t)$ into the sum of statistically-independent, zero-mean, Gaussian-distributed contributions, $\{E_m(t)\}$, from its $M \sim a_0^2/\rho_0^2 \gg 1$, radius- ρ_0 , centers at $\{\rho_m : 1 \leq m \leq M\}$, coherence areas. In terms of these contributions we have that

$$E_b(\rho_b, t) \approx T(\rho_b) \sum_{m=1}^M E_m(\rho_b, t) \tag{67}$$

and

$$E_p(\rho_p, t) \approx \sum_{m=1}^M E_m(\rho_p, t), \tag{68}$$

where

$$E_m(\rho, t) \equiv E_m(t - L/c) h_L(\rho - \rho_m) \pi \rho_0^2. \tag{69}$$

Now we have that

$$\begin{aligned}
 G_{bp}^{(2)}(\boldsymbol{\rho}_b, t; \boldsymbol{\rho}_p, t) &\approx \left\langle \sum_{m=1}^M |T(\boldsymbol{\rho}_b)|^2 |E_m(\boldsymbol{\rho}_b, t)|^2 \sum_{m'=1}^M |E_{m'}(\boldsymbol{\rho}_p, t)|^2 \right. \\
 &\quad + \sum_{m=1}^M T^*(\boldsymbol{\rho}_b) E_m^*(\boldsymbol{\rho}_b, t) E_m(\boldsymbol{\rho}_p, t) \\
 &\quad \left. \times \sum_{m'=1}^M T(\boldsymbol{\rho}_b) E_{m'}(\boldsymbol{\rho}_b, t) E_{m'}^*(\boldsymbol{\rho}_p, t) \right\rangle \tag{70} \\
 &= \left\langle \sum_{m=1}^M \sum_{m'=1}^M \left| \frac{T(\boldsymbol{\rho}_b)}{\sqrt{2}} [E_m(\boldsymbol{\rho}_b, t) E_{m'}(\boldsymbol{\rho}_p, t) \right. \right. \\
 &\quad \left. \left. + E_{m'}(\boldsymbol{\rho}_b, t) E_m(\boldsymbol{\rho}_p, t)] \right|^2 \right\rangle, \tag{71}
 \end{aligned}$$

where the independent, zero-mean nature of the fields contributed by pseudothermal source’s different coherence areas has been employed to eliminate terms in which phase-randomness is present, and $M \gg 1$ has been used to ignore the double counting of the M terms with $m = m'$ because the extra contribution is small in comparison with the $M(M - 1)$ terms with $m \neq m'$.

If we complete the averaging in Eq. (70), again using $M \gg 1$ to ignore the double counting of the $m = m'$ terms, we get

$$\begin{aligned}
 G_{bp}^{(2)}(\boldsymbol{\rho}_b, t; \boldsymbol{\rho}_p, t) &\approx \sum_{m=1}^M |T(\boldsymbol{\rho}_b)|^2 \langle |E_m(\boldsymbol{\rho}_b, t)|^2 \rangle \sum_{m'=1}^M \langle |E_{m'}(\boldsymbol{\rho}_p, t)|^2 \rangle \\
 &\quad + |T(\boldsymbol{\rho}_b)|^2 \left| \sum_{m=1}^M \langle E_m^*(\boldsymbol{\rho}_b, t) E_m(\boldsymbol{\rho}_p, t) \rangle \right|^2. \tag{72}
 \end{aligned}$$

Inserting Eq. (72) into Eq. (62) gives the expected result: the first term on the right in Eq. (72) produces a featureless background, and the second term yields the ghost image. Moreover, that ghost image will have the field-of-view and spatial resolution that we derived by a more exact calculation in Sect. 3.2, because both there and here those characteristics are governed by propagation of the pseudothermal source’s phase-insensitive coherence.

Having seen that the coherence-area approximation can reproduce the pseudothermal ghost-imaging behavior we derived earlier, we return to Eq. (71) to give that image its two-photon interference interpretation. The field expression inside the squared magnitude in this equation is the superposition of two terms. In the first, we have the product of the field at $\boldsymbol{\rho}_b$ on the transmission mask that originates from the source’s m th coherence area multiplied by the field at $\boldsymbol{\rho}_p$ on the pinhole detector that is due to the source’s m' th coherence area. In the second term, we have the physically indistinguishable situation in which the field at $\boldsymbol{\rho}_b$ from the m' th coherence area

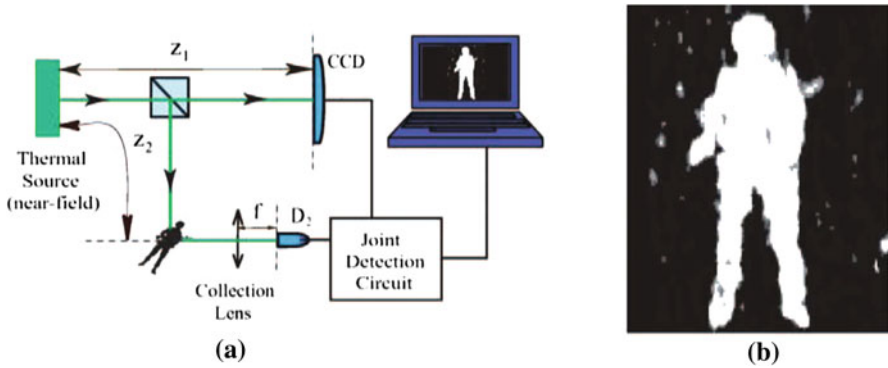


Fig. 9 First demonstration of ghost imaging in reflection [19]: **a** table-top experimental setup using a pseudothermal source, a CCD array for the high-spatial-resolution reference measurement, and photon coincidence-counting with the output from the bucket detector; **b** ghost image of the toy-soldier object measured in reflection

is multiplied by the field at ρ_p originating at the source's m th coherence area. We have presumed operation at low enough flux that the photocurrent cross-correlation in Fig. 8 is equivalent to photon-coincidence counting, thus the preceding coherence-area field contributions can be taken to be due to single photons when thought of quantum mechanically. So, just as we argued from the biphoton analysis of the SPDC case, these pseudothermal terms can be interpreted as originating from nonlocal two-photon interference.

5 Other ghost-imaging configurations

Sections 3 and 4 provided a detailed treatment of ghost imaging in transmission with single-wavelength sources. In the present section we will present briefer developments of other ghost imaging configurations. We will start with ghost imaging in reflection, done with a single-wavelength source, focusing on the effects of target-induced speckle associated with imaging rough-surfaced targets. Here we will only consider pseudothermal operation, because the quasi-Lambertian nature of rough-surface reflection places a premium on the use of high-flux sources in standoff-sensing applications. Standoff sensing over terrestrial paths inevitably encounters atmospheric turbulence, so we will allow for its random propagation impairments in our treatment. We then move on to computational ghost imaging, in which the pseudothermal source is replaced with a deterministic illuminator that permits a ghost image to be formed using a computed reference field, i.e., with only a bucket detector. In addition to our theory development, we will also include discussion of recent table-top experimental work for all three of these topics: ghost imaging in reflection, the impact of turbulence on ghost imaging, and computational ghost imaging. Finally, we shall return to SPDC operation to examine the merits of two-wavelength operation for ghost imaging in transmission.

5.1 Ghost imaging in reflection for standoff sensing

The prospect that ghost imaging might find useful application as an alternative to a more conventional laser radar—or other active imager¹⁸—for standoff sensing was significantly increased when Meyers et al. reported the first demonstration of ghost imaging done in reflection [19]. Their table-top experiment, whose schematic setup is shown in Fig. 9a, was a lensless, pseudothermal configuration that was operated at sufficiently low flux that photon coincidence-counting could be employed. The resulting ghost image of the toy-soldier object is shown in Fig. 9b. This ghost image was obtained when the source-to-reference (CCD) detector distance z_1 equaled the source-to-object distance z_2 , so that the identical classical fields emerging from the beam splitter in Fig. 9a cast identical speckle patterns at these locations, in keeping with the speckle-correlation interpretation of pseudothermal ghost imaging we have described for transmissive configurations. It should be noted, however, that Meyers et al. interpreted their pseudothermal ghost image formed in reflection as being a consequence of two-photon interference, and argued that it could *not* be explained by correlations between classical intensity fluctuations. But, as we have shown in Sect. 4, both explanations are valid descriptions of pseudothermal ghost imaging.

Meyers and Deacon took a second significant step toward ghost imaging as a stand-off sensor when they explored the vulnerability of reflective ghost imaging to atmospheric turbulence [21]. Atmospheric turbulence refers to the few parts-per-million spatiotemporal refractive-index fluctuations that accompany turbulent mixing of air parcels with ~ 1 K temperature differences. These fluctuations, occurring on spatial scales ranging from 10^{-3} to 10^2 m, evolve in time and drift with prevailing winds producing temporal variations on the order of 1–10 ms [47–49]. They have long been the bane of earth-bound astronomers, and they limit the spatial resolution of laser radars. Thus it is particularly germane to understand the effect of turbulence on ghost imaging.

Figure 10 sketches the table-top experimental setup from [21]. The beam-split outputs from a pseudothermal source illuminated an “ARL” pattern and an adjacent sheet of glossy white paper. The reflected light from these two illumination patterns were collected by different sections of a CCD array that was arranged to provide bucket detection of the light reflected by the ARL pattern and reference detection of the other light. Operation was at low flux levels in photon-counting mode, and the ghost image was obtained by gating the reference arm when photodetection events were registered by the bucket detector on the signal arm. To create strong turbulence, heating elements could be inserted at any and all of the locations shown in this figure. A conventional image of the ARL pattern was also formed by using the CCD’s imaging capability on the light reflected from the ARL pattern.

Results from the Meyers and Deacon experiments were somewhat surprising. Figure 11a contains three conventional short-exposure images of the “R” from the ARL pattern, showing distortions created by the presence of turbulence. The left image in Fig. 11b shows an ARL ghost image taken without atmospheric turbulence,

¹⁸ An active imager is one that provides its own object illumination, rather than relying on ambient light for this purpose.

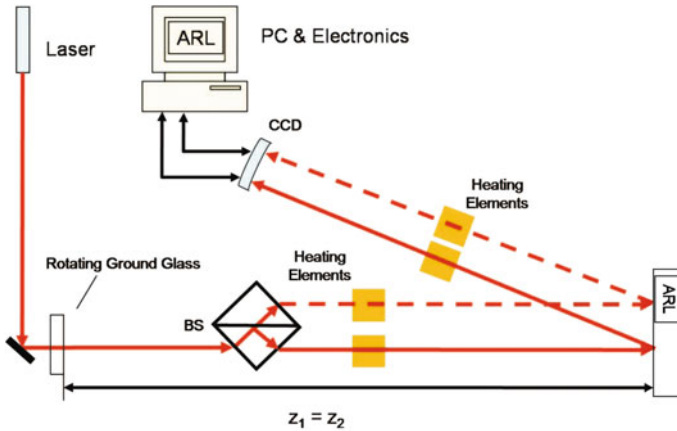


Fig. 10 Table-top experimental setup for probing the sensitivity of reflective ghost imaging to atmospheric turbulence [21]

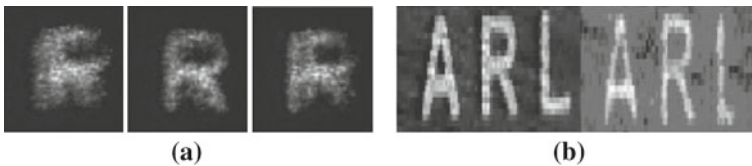


Fig. 11 Experimental results from [21]: **a** three short-exposure conventional images of the “R” from the ARL pattern in the presence of turbulence; **b** ghost images taken of the ARL pattern in the absence (*left*) and the presence (*right*) of turbulence

while the right image in that figure shows an ARL ghost image taken in the presence of turbulence. Because they used turbulence whose strength parameter was as strong as $C_n^2 = 10^{-9} \text{ m}^{-2/3}$, Meyers and Deacon concluded that ghost imaging is intrinsically *immune* to atmospheric turbulence. This conclusion is at odds with theoretical work of Cheng [22], who showed that lensless pseudothermal ghost imaging in transmission suffers from turbulence-limited resolution loss when the atmospheric coherence length at the source becomes smaller than the source’s intensity radius. Hence it is incumbent upon us to see whether Cheng’s analysis extends to the reflective case. In conjunction with such an assessment, we must also confront the fact that most scenes of interest for standoff sensing are comprised of objects whose surfaces are rough on the scale of optical wavelengths. Laser light reflected from such surfaces project speckle patterns [45] akin to those we have noted arise from propagation through ground-glass diffusers. Hence target-induced speckle must be included—in addition to atmospheric turbulence—in any consideration of ghost imaging for standoff sensing. Joint consideration of reflective ghost imaging with rough-surfaced objects and atmospheric turbulence will comprise the rest of this subsection, where we will draw upon theoretical results from [23,24].

Our theoretical development will assume the pseudothermal lensless configuration shown in Fig. 12. In this arrangement, the output from a pseudothermal source is

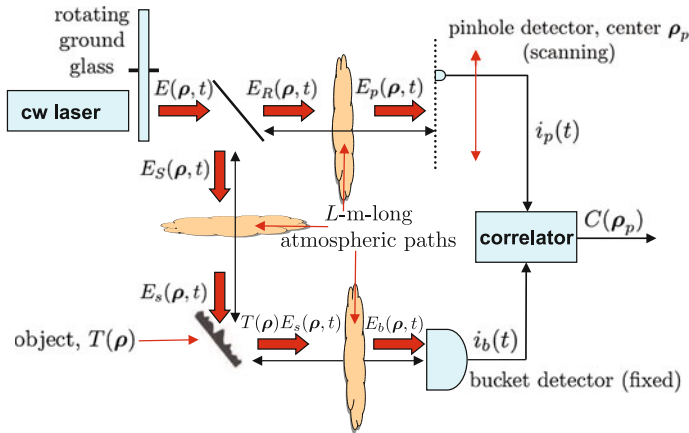


Fig. 12 Configuration for lensless ghost imaging in reflection using a pseudothermal source with atmospheric turbulence potentially present in all propagation paths

divided by a 50–50 beam splitter. After propagation over an L -m-long atmospheric path, one of the beam splitter’s output beams illuminates a rough-surfaced object with field-reflection coefficient $T(\rho)$. After propagation over a different L -m-long atmospheric path, the beam splitter’s other output beam illuminates a scanning-pinhole detector. The light reflected from the object is collected by a bucket detector after propagation over yet another L -m-long atmospheric path. The bucket and scanning-pinhole detectors’ photocurrents are then cross correlated to obtain

$$C(\rho_p) = \frac{1}{T_I} \int_{-T_I/2}^{T_I/2} dt i_b(t) i_p(t - L/c), \tag{73}$$

which is supposed to yield a ghost image of the object.

Before proceeding further, several clarifying comments are in order. The first such comment has to do with our including turbulence on the reference path. We expect turbulence to be a deleterious influence, at best, on ghost-imaging performance. So a ghost imager for standoff sensing would very likely use a lens to cast an image of the far-field reference light onto a scanning pinhole (or a CCD array) inside a controlled (turbulence-free) environment. Our allowing an outdoor path avoids the necessity of accounting for ghost-image minification. Moreover, all three atmospheric paths in Fig. 12 will be taken to be sufficiently separated that their refractive-index fluctuations are statistically independent. Thus we can turn off the turbulence on the reference path, if desired, in our analysis to better represent what would be done in practice. The second point to note concerns Eq. (73), where we have imposed an L/c propagation delay in the bucket photocurrent so that it is being cross correlated with the scanning-pinhole photocurrent associated with the same speckle pattern cast by the pseudothermal source. Finally, we need to provide a statistical characterization for $T(\rho)$. In our treatment of the transmissive case, we took the object to be deterministic;

for the reflective case we need a random-process characterization. Here we shall use what is commonly assumed in laser radar analyses [50]: $T(\boldsymbol{\rho})$ is a zero-mean, complex-valued, Gaussian random process whose statistics at illumination wavelength λ_0 are completely specified by¹⁹

$$\langle T^*(\boldsymbol{\rho}_1)T(\boldsymbol{\rho}_2) \rangle = \lambda_0^2 \mathcal{T}(\boldsymbol{\rho}_1)\delta(\boldsymbol{\rho}_1 - \boldsymbol{\rho}_2). \tag{74}$$

Here, $\mathcal{T}(\boldsymbol{\rho})$ is the object’s average intensity-reflection coefficient, which is the quantity that we will try to image with the Fig. 12 setup.

Paralleling the development in Sect. 3.2, we will use the ensemble average, $\langle C(\boldsymbol{\rho}_p) \rangle$, to determine the spatial resolution of the reflective ghost image in the presence of turbulence. We shall assume that the scanning-pinhole detector’s photosensitive region is smaller than the speckle size in its illumination, that the photodetectors are AC coupled with output bandwidths well in excess of the temporal variations produced by both the rotating ground glass and atmospheric turbulence. There are three statistically-independent sources of randomness in the Fig. 12 setup: the pseudothermal light, the atmospheric turbulence (itself comprised of independent refractive-index fluctuations on the three propagation paths), and the object’s field-reflection coefficient $T(\boldsymbol{\rho})$. Thus $\langle C(\boldsymbol{\rho}_p) \rangle$ is easily obtained by means of iterated expectation. Specifically, we first find its value conditioned on knowledge of the turbulence and the object, then we average over the object statistics, and finally we average over the turbulence statistics. The details are available in [23,24], so here we will limit ourselves to describing how the turbulence is accounted for and then present our $\langle C(\boldsymbol{\rho}_p) \rangle$ expression.

Consider propagation over an L -m-long atmospheric path whose input field, at $z = 0$, is $E_0(\boldsymbol{\rho}, t)$, and whose output field, at $z = L$, is $E_L(\boldsymbol{\rho}', t)$. In the absence of turbulence, the propagation is governed by the Huygens–Fresnel principle from Sect. 2.3. In the presence of turbulence, it is characterized by the extended Huygens–Fresnel principle, see Chap. 5 of [48]:

$$E_L(\boldsymbol{\rho}', t) = \int d\boldsymbol{\rho} E_0(\boldsymbol{\rho}, t - L/c)h_L(\boldsymbol{\rho}' - \boldsymbol{\rho})e^{\chi(\boldsymbol{\rho}', \boldsymbol{\rho}, t) + i\phi(\boldsymbol{\rho}', \boldsymbol{\rho}, t)}, \tag{75}$$

where the free-space Green’s function h_L is given by Eq. (31), and the real-valued random processes $\chi(\boldsymbol{\rho}', \boldsymbol{\rho}, t)$ and $\phi(\boldsymbol{\rho}', \boldsymbol{\rho}, t)$ represent the log-amplitude and phase fluctuations imposed on $E_L(\boldsymbol{\rho}', t)$ when $E_0(\boldsymbol{\rho}, t)$ is a point-source emission from $\boldsymbol{\rho}$ at time $t - L/c$. Physically, this says that the presence of turbulence changes the Green’s function for L m of propagation from $h_L(\boldsymbol{\rho}' - \boldsymbol{\rho})$ to $h_L(\boldsymbol{\rho}' - \boldsymbol{\rho})e^{\chi(\boldsymbol{\rho}', \boldsymbol{\rho}, t) + i\phi(\boldsymbol{\rho}', \boldsymbol{\rho}, t)}$. It turns out that the only turbulence statistic needed to obtain $\langle C(\boldsymbol{\rho}_p) \rangle$ is the correlation

¹⁹ Strictly speaking, these statistics do not correctly account for the reflected field’s behavior until sufficient propagation away from the object has occurred that the Central Limit Theorem can be invoked, cf. our discussion of the use of Gaussian statistics for the pseudothermal source. As a practical matter, the necessary far-field condition will be satisfied in standoff-sensing applications.

function²⁰

$$\left\langle e^{\chi(\boldsymbol{\rho}', \boldsymbol{\rho}_1, t) - i\phi(\boldsymbol{\rho}', \boldsymbol{\rho}_1, t)} e^{\chi(\boldsymbol{\rho}', \boldsymbol{\rho}_2, t) + i\phi(\boldsymbol{\rho}', \boldsymbol{\rho}_2, t)} \right\rangle = e^{-D(\boldsymbol{\rho}_1 - \boldsymbol{\rho}_2)/2} \tag{76}$$

where

$$D(\boldsymbol{\rho}) \equiv (|\boldsymbol{\rho}|/\rho_T)^{5/3} \tag{77}$$

with $C_n^2(z)$ being the turbulence-strength profile along the path from $z = 0$ to $z = L$, and

$$\rho_T \equiv \left(2.91k_0^2 \int_0^L dz C_n^2(z)(1 - z/L)^{5/3} \right)^{-3/5} \tag{78}$$

being the source-plane coherence length of the turbulence. For the Fig. 12 configuration there will be three such coherence lengths: one for the signal-to-object path, one for the object-to-bucket path, and one for the reference-to-pinhole path. These will be denoted ρ_{so} , ρ_{ob} , and ρ_{rp} , respectively. All will be assumed to be much larger than the pseudothermal source’s ρ_0 coherence radius,²¹ but they may be smaller or larger than that source’s intensity radius a_0 .

Under the assumptions we have made, the intensity radius of the light reaching the object in Fig. 12 will continue to be $a_L = \lambda_0 L/\rho_0$, so that taking $\mathcal{T}(\boldsymbol{\rho})$ to be nonzero only for $|\boldsymbol{\rho}| \ll a_L$ and using the square-law approximation

$$D(\boldsymbol{\rho}) \approx (|\boldsymbol{\rho}|/\rho_T)^2 \tag{79}$$

in lieu of Eq. (77), we get the closed-form result

$$\langle C(\boldsymbol{\rho}_p) \rangle = q^2 \eta^2 A_p \left(\frac{2P}{\pi a_L^2} \right)^2 \frac{A_b \rho_L^2}{L^2 \rho_L^2} \int d\boldsymbol{\rho} \mathcal{T}(\boldsymbol{\rho}) e^{-|\boldsymbol{\rho} - \boldsymbol{\rho}_p|^2/\rho_L^2}, \tag{80}$$

with A_b being the bucket detector’s photosensitive area and

$$\rho'_L \equiv \rho_L \sqrt{\frac{2\rho_{rp}^2 \rho_{so}^2 + a_0^2(\rho_{rp}^2 + \rho_{so}^2)}{2\rho_{rp}^2 \rho_{so}^2}}. \tag{81}$$

²⁰ Although originally derived via the Rytov (weak-perturbation) approximation, this correlation function has a more general derivation whose validity includes the strong-perturbation regime, wherein saturated scintillation occurs [49]. Both derivations use the Kolmogorov 11/3-law spatial spectrum for the refractive-index fluctuations. Strictly speaking, this limits the validity of Eq. (77) to $|\boldsymbol{\rho}|$ between the inner scale (~ 1 mm) and the outer scale (~ 10 – 10^2 m) of the turbulence.

²¹ The ground-glass diffuser will make ρ_0 comparable to the laser wavelength; atmospheric turbulence leads to coherence lengths on the order of centimeters.

Here we see that the average AC-coupled ghost image is proportional to the rough-surfaced object’s average intensity-reflection coefficient $\mathcal{T}(\boldsymbol{\rho})$ convolved with a Gaussian point-spread function of spatial resolution ρ'_L .

It is instructive to compare Eq. (80) for pseudothermal reflective ghost imaging in the presence of turbulence to

$$\langle C(\boldsymbol{\rho}_p) \rangle = q^2 \eta^2 A_p \left(\frac{2P}{\pi a_L^2} \right)^2 \int_{A_b} d\boldsymbol{\rho} e^{-|\boldsymbol{\rho} - \boldsymbol{\rho}_p|^2 / \rho_L^2} |T(\boldsymbol{\rho})|^2, \tag{82}$$

which is the corresponding result for pseudothermal transmissive ghost imaging in the absence of turbulence. The former differs from the latter in three ways. First, it is imaging $\mathcal{T}(\boldsymbol{\rho})$ rather than $|T(\boldsymbol{\rho})|^2$, as expected from our statistical model for the rough-surfaced object. Second, the quasi-Lambertian nature of reflection from that rough-surfaced object leads to the $A_b/L^2 \ll 1$ angular-subtense factor in the reflective case, representing the fraction of the reflected light that is collected by the bucket detector. Third, the no-turbulence $e^{-|\boldsymbol{\rho}|^2/\rho_L^2}$ point-spread function is replaced by the turbulence-degraded point-spread function $(\rho_L/\rho'_L)^2 e^{-|\boldsymbol{\rho}|^2/\rho_L^2}$. It is this third difference, which was previously found by Cheng [22] for transmissive ghost imaging, that deserves the most attention.

Equation (81) shows that turbulence between the object and the bucket detector in Fig. 12 has no effect on the average ghost image. This is a consequence of the turbulence coherence length for that propagation path being much larger than the coherence length of $T(\boldsymbol{\rho})$. More importantly, Eq. (81) indicates that turbulence in the reference-to-pinhole and signal-to-object paths both degrade the reflective ghost image’s spatial resolution when they become sufficiently small. In particular, if we assume that $\rho_{so} = \rho_{rp} = \rho_T$, as will be the case for horizontal paths with uniform C_n^2 profiles, then we get

$$\frac{\rho'_L}{\rho_L} = \sqrt{1 + a_0^2/\rho_T^2} \approx \begin{cases} 1, & \text{for } \rho_T \gg a_0 \\ a_0^2/\rho_T^2 \gg 1, & \text{for } \rho_T \ll a_0. \end{cases} \tag{83}$$

Just as Cheng found for the transmissive case, turbulence degrades ghost image resolution when its coherence length is smaller than the source’s intensity radius. Whether or not this theoretical conclusion contradicts the experiments of Meyers and Deacon cannot be determined from [21], because these authors did not report the values of the relevant parameters, viz., their source’s intensity radius and the source-plane turbulence coherence length. In this regard it is worth discussing the recent paper by Dixon et al. [51], which does report turbulence-degraded imagery for an SPDC experiment—performed in transmission—in which the relevant turbulence coherence length was measured.

Dixon et al. used the setup shown in Fig. 13. The SPDC crystal was located at spatial shift Δ from the central image plane of two $4f$ imaging systems: one for the signal beam and one for the idler. At the signal-beam image plane there was a one-dimensional sinusoidal transmission mask, $T(x) = \cos(k_m x)$, of spatial frequency

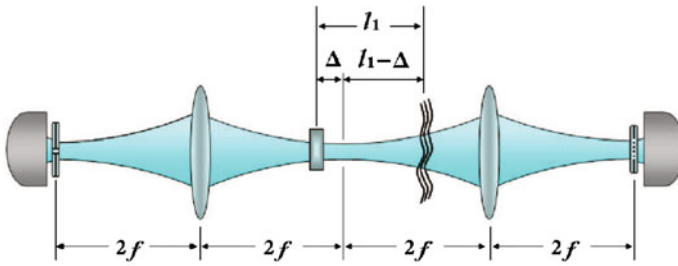


Fig. 13 Unfolded configuration for the Dixon et al. table-top experiment [51] testing the sensitivity of SPDC ghost imaging to turbulence. The signal-beam path is on the *right*; the idler-beam path in on the *left*. The former leads to a one-dimensional sinusoidal image-plane transmission mask followed by a bucket detector; the latter leads to an image-plane scanning-slit detector

k_m , followed by a bucket detector. At the idler-beam image plane there was a scanning-slit detector. A heat gun was used to create turbulence in the signal-beam path between the downconverter and the imaging lens. Assuming that the lens diameters are large enough that they capture all the light from the SPDC source, and that the turbulence is confined to a narrow sheet a distance ℓ_1 from the SPDC crystal, biphoton theory predicts that the transmission mask's

$$|T(x)|^2 = \frac{1 + \cos(2k_m x)}{2} \tag{84}$$

sinusoidal intensity transmission will be ghost-imaged in photon coincidence as

$$\langle C(x) \rangle \propto e^{-2x^2/a_0^2} [1 + \gamma \cos(2k_m x)], \tag{85}$$

where

$$\gamma \equiv \gamma_0 e^{-2k_m^2(\ell_1 - \Delta)^2 / \rho_0^2 k_0^2} \tag{86}$$

gives the fringe visibility, with γ_0 being its no-turbulence value, and we have converted the notation from [51] to match that of the present paper.

Figure 14 plots the measured fringe visibility γ versus the distance ℓ_1 between the SPDC crystal and the turbulence for unshifted ($\Delta = 0$) and shifted ($\Delta = 330$ mm) configurations. As predicted by Eq. (86), the shifted configuration is less sensitive to turbulence than is the unshifted case, with the former having substantial immunity when the turbulence is located at or near the central image plane. More importantly, although the Dixon et al. experiments do not match the Fig. 12 configuration, they clearly show that ghost imaging is *not* intrinsically immune to the effects of atmospheric turbulence.

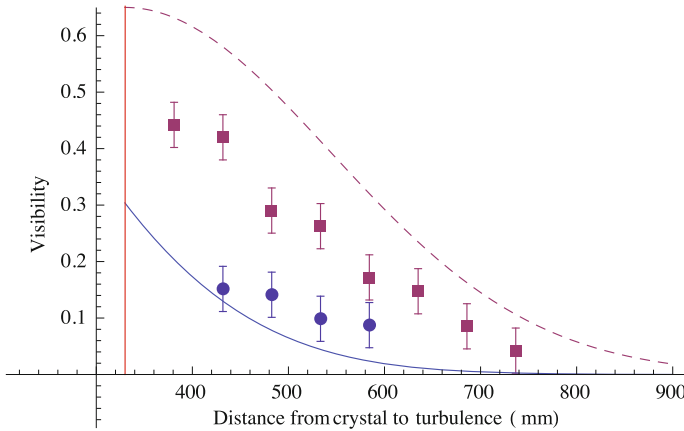


Fig. 14 Fringe visibility versus crystal-to-turbulence distance ℓ_1 obtained by Dixon et al. using the setup shown in Fig. 13. The blue-circle data is for $\Delta = 0$ and the red-square data is for $\Delta = 330$ mm. The theoretical fits are plotted from Eq. (86) using $\gamma_0 = 1$ for $\Delta = 0$, $\gamma_0 = 0.65$ for $\Delta = 330$ mm, and the measured $\rho_0 = 0.71$ mm value. The central image plane is indicated by the vertical red line for the shifted ($\Delta = 330$ mm) case (Color figure online)

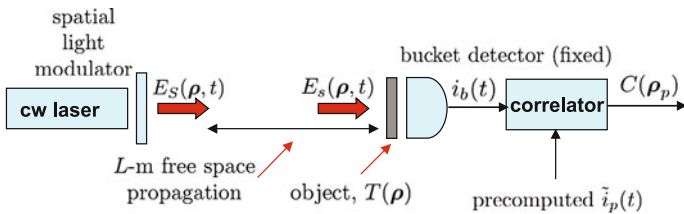


Fig. 15 Configuration for lensless computational ghost imaging in transmission. Not shown is $E_b(\rho, t) = T(\rho)E_s(\rho, t)$, the field illuminating the bucket detector

5.2 Computational ghost imaging

The basic paradigm in pseudothermal ghost imaging is to use a time-varying (rotating ground-glass) diffuser to convert a spatially-coherent laser beam into one with low spatial coherence and moderate temporal bandwidth that, after 50–50 beam splitting, will cast identical speckle patterns on the object to be imaged and a high-spatial-resolution reference detector. The ghost image then emerges in the photocurrent cross correlation between the output from the high-spatial-resolution detector and that from a single-pixel (bucket) detector which collects light transmitted through or reflected from the object. In [16] it was argued that the ground-glass diffuser could be replaced with a spatial light modulator (SLM) whose individual pixels were driven by statistically-independent noise sources. From there it was easy to extrapolate to the computational ghost-imaging concept, shown for the transmissive case without turbulence, in Fig. 15. In this concept, deterministic modulation applied to the SLM’s pixels produces a classical field $E_S(\rho, t)$ that results in a computable—from the Huygens–Fresnel principle—field $E_s(\rho, t)$ at the transmission mask $T(\rho)$. Making use of that computed field we can cross correlate the AC-coupled output of the bucket detector with

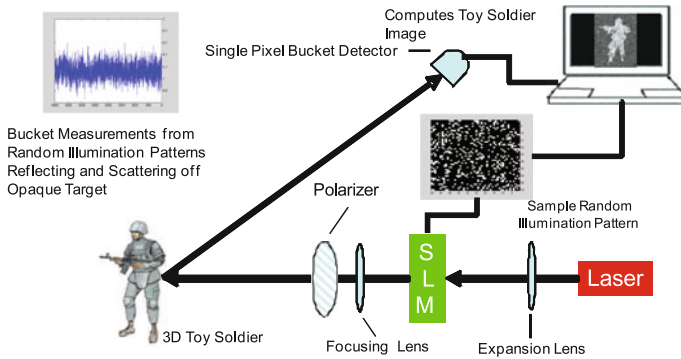


Fig. 16 Configuration for CS computational ghost imaging of a toy soldier in reflection [21]. The computer uses the known sequence of illumination patterns and the single-photon bucket detections to obtain the image

$$\tilde{i}_p(t) \equiv q\eta A_p |E_s(\boldsymbol{\rho}_p, t)|^2, \tag{87}$$

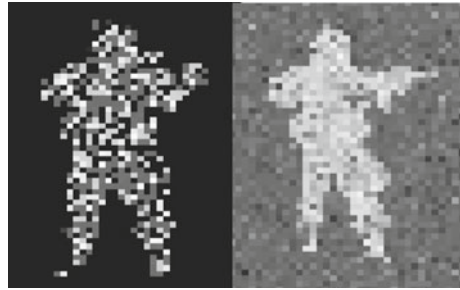
to obtain a ghost image. Physically, $\tilde{i}_p(t)$ corresponds to the average photocurrent from a pinhole detector at $\boldsymbol{\rho}_p$ conditioned on knowledge of its illumination, i.e., the photocurrent from a real pinhole detector with its shot noise suppressed. Thus if the SLM produces time-varying $|E_s(\boldsymbol{\rho}, t)|^2$ patterns covering a radius- a_L region with radius- ρ_L speckles, we should expect this cross correlation to behave, on average, very much like the AC-coupled pseudothermal ghost image formed with the two-detector configuration from Fig. 8.

Computational ghost imaging was first demonstrated by Bromberg et al. [25]. That group later replaced the correlator in Fig. 15 with a compressive-sensing processor [26]. Compressive sensing exploits the sparseness of object scenes in an appropriate basis to achieve accurate reconstructions with many fewer samples—in this case SLM patterns—than a conventional correlator approach, requires.²² Indeed, viewed this way, computational ghost imaging with compressive sensing (CS) is known and has been studied in the signal-processing community as the structured illumination version of the CS single-pixel camera [53].

Meyers and Deacon [21] have pushed beyond the compressive-sensing version of computational ghost imaging in transmission, by applying the CS approach to image a toy soldier in reflection, as sketched in Fig. 16. Sample results from their experiments are shown in Fig. 17. The image on the left was obtained by randomly scanning a single illumination point across the region containing the toy soldier, whereas the image on the right was obtained by simultaneous random scanning of three illumination points across that object region. Because the Fig. 16 processor knew, in both cases, what object-region points were being illuminated, the image on the left is easily understood in conventional laser radar terms. In particular, the spatial resolution obtained from a laser radar depends on both its transmitter and its receiver antenna patterns. A bucket-detector receiver affords no spatial resolution in the conventional laser radar sense.

²² See [52] for a tutorial overview of compressive sensing.

Fig. 17 CS computational ghost images of the toy soldier obtained using the setup from Fig. 16. The *left* image was obtained with randomly scanned single-pixel illumination; the *right* image was obtained with randomly scanned three-pixel illumination



However, when used in conjunction with a narrow-beam transmitter that is aimed at a known location on the object, the bucket detector's output provides a measure of the reflection strength within that small illuminated region. On the other hand, the image on the right in Fig. 17 is a CS computational ghost image, because individual bucket-detector outputs do *not* directly yield reflection-strength information for a single pixel on the toy soldier.

5.3 Two-wavelength SPDC ghost imaging

For the final ghost-imaging configuration we shall discuss, we return to the SPDC setup for lensless ghost imaging. Every two-detector (pinhole-plus-bucket) case we have considered so far has assumed single-wavelength operation. In Sect. 3.1 that meant our downconversion source was operated at frequency degeneracy; in Sects. 3.2 and 5.1 single-wavelength operation was a natural consequence of signal and reference light being derived from 50–50 beam splitting of a single randomly-diffused laser beam. Now we shall address ghost imaging with an SPDC source whose signal and idler wavelengths are quite disparate. There is good motivation for such consideration. High-spatial-resolution detectors are not available at all wavelengths, including many in the infrared where atmospheric turbulence and scattering effects can be more benign than in the visible region. Thus, using a downconversion source whose idler wavelength has good CCD-array technology and a signal wavelength with desirable atmospheric propagation characteristics can yield the best of both these worlds. This is accomplished by keeping the reference (idler) path inside a controlled environment—using a lens to cast its far-field speckle pattern onto a focal-plane CCD array—and using the signal light to interrogate the object through an atmospheric propagation path. Prior work on two-wavelength ghost imaging includes [27–29]. We shall content ourselves with applying Gaussian-state analysis to determine the field-of-view and spatial resolution achieved with the two-wavelength lensless SPDC imager shown in Fig. 18.

For our analysis of the two-wavelength case we shall make the same source assumptions as in Sect. 3.1: the downconverter's signal and idler beam are in a zero-mean, jointly Gaussian state whose phase-insensitive auto-covariances are given by the Gaussian-Schell model expressions from Sect. 2.1 and whose phase-sensitive cross-covariance is given by the low-brightness term (the second term) from Eq. (12). We

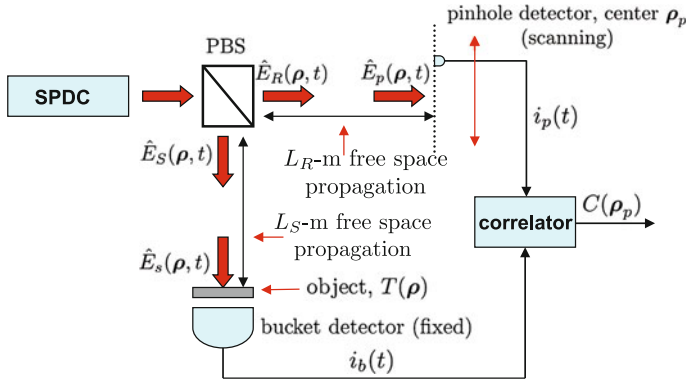


Fig. 18 Configuration for lensless ghost imaging of a transmission mask with a two-wavelength SPDC source. Not shown is $\hat{E}_b(\boldsymbol{\rho}, t) = T(\boldsymbol{\rho})\hat{E}_s(\boldsymbol{\rho}, t) + \sqrt{1 - |T(\boldsymbol{\rho})|^2} \hat{E}_{sv}(\boldsymbol{\rho}, t)$, the quantum field that illuminates the bucket detector, where $\hat{E}_{sv}(\boldsymbol{\rho}, t)$ is a vacuum-state field operator needed to preserve commutator brackets in the presence of transmission loss through the mask $T(\boldsymbol{\rho})$

will also assume that both the signal and reference paths in Fig. 18 are long enough that far-field propagation applies at the signal and reference wavelengths, λ_S and λ_R , respectively. Finally, as in Sect. 3.1, we will make the small- A_p assumption and take the photodetectors to be DC coupled with quantum efficiency η and output filter bandwidth Ω_B whose reciprocal is much greater than the downconverter’s coherence time T_0 . It then follows that the ensemble-average photocurrent cross-correlation is

$$\langle C(\boldsymbol{\rho}_p) \rangle = q^2 \eta^2 \mathcal{A}_p \left(\mathcal{K}_{\hat{E}_p \hat{E}_p}^{(n)}(\boldsymbol{\rho}_p, \boldsymbol{\rho}_p) \int_{\mathcal{A}_b} d\boldsymbol{\rho} \mathcal{K}_{\hat{E}_s \hat{E}_s}^{(n)}(\boldsymbol{\rho}, \boldsymbol{\rho}) |T(\boldsymbol{\rho})|^2 + \frac{\Omega_B T_0}{4\sqrt{2}} \int_{\mathcal{A}_b} d\boldsymbol{\rho} |\mathcal{K}_{\hat{E}_s \hat{E}_p}^{(p)}(\boldsymbol{\rho}, \boldsymbol{\rho}_p)|^2 |T(\boldsymbol{\rho})|^2 \right), \tag{88}$$

where, using the far-field conditions, we have

$$\mathcal{K}_{\hat{E}_p \hat{E}_p}^{(n)}(\boldsymbol{\rho}_p, \boldsymbol{\rho}_p) = \frac{2P}{\pi a_0^2} \int d\boldsymbol{\rho}_1 \int d\boldsymbol{\rho}_2 \frac{e^{-(|\boldsymbol{\rho}_1|^2 + |\boldsymbol{\rho}_2|^2)/a_0^2 - |\boldsymbol{\rho}_1 - \boldsymbol{\rho}_2|^2/2\rho_0^2} e^{ik_R \boldsymbol{\rho}_p \cdot (\boldsymbol{\rho}_1 - \boldsymbol{\rho}_2)/L_R}}{(\lambda_R L_R)^2}, \tag{89}$$

$$\mathcal{K}_{\hat{E}_s \hat{E}_s}^{(n)}(\boldsymbol{\rho}, \boldsymbol{\rho}) = \frac{2P}{\pi a_0^2} \int d\boldsymbol{\rho}_1 \int d\boldsymbol{\rho}_2 \frac{e^{-(|\boldsymbol{\rho}_1|^2 + |\boldsymbol{\rho}_2|^2)/a_0^2 - |\boldsymbol{\rho}_1 - \boldsymbol{\rho}_2|^2/2\rho_0^2} e^{ik_S \boldsymbol{\rho} \cdot (\boldsymbol{\rho}_1 - \boldsymbol{\rho}_2)/L_S}}{(\lambda_S L_S)^2}, \tag{90}$$

and

$$\begin{aligned}
 |\mathcal{K}_{\hat{E}_s \hat{E}_p}^{(p)}(\boldsymbol{\rho}, \boldsymbol{\rho}_p)|^2 &= \left(\frac{2P}{\pi a_0^2} \right)^2 \sqrt{\frac{2}{\pi}} \frac{a_0^2}{PT_0 \rho_0^2} \left| \int d\boldsymbol{\rho}_1 \int d\boldsymbol{\rho}_2 \right. \\
 &\quad \times \frac{e^{-(|\boldsymbol{\rho}_1|^2 + |\boldsymbol{\rho}_2|^2)/a_0^2 - |\boldsymbol{\rho}_1 - \boldsymbol{\rho}_2|^2/\rho_0^2} e^{-ik_S \boldsymbol{\rho}_1/L_S} e^{-ik_R \boldsymbol{\rho}_p \cdot \boldsymbol{\rho}_2/L_R}}{\lambda_S L_S \lambda_R L_R} \Big|^2, \tag{91}
 \end{aligned}$$

with $k_S \equiv 2\pi/\lambda_S$ and $k_R \equiv 2\pi/\lambda_R$ being the wave numbers at the signal and reference wavelengths.

The task of evaluating the integrals in Eqs. (89)–(91)—and, more importantly, choosing the path lengths L_S and L_R to optimize the resulting spatial resolution—is simplified by imposing the condition $\lambda_S L_S = \lambda_R L_R$, which implies that $k_S/L_S = k_R/L_R$. Then, defining $\bar{\lambda}L = \lambda_S L_S = \lambda_R L_R$ reduces the integrals in Eqs. (89)–(91) to those evaluated in Sect. 3.1 if we substitute $\bar{\lambda}L$ for $\lambda_0 L$, $\bar{a}_L = \bar{\lambda}L/\pi\rho_0$ for a_L , and $\bar{\rho}_L = \bar{\lambda}L/\pi a_0$ for ρ_L . Furthermore, the comments concerning depth-of-focus that were made at the conclusion of Sect. 3 guarantee that choosing $\lambda_S L_S = \lambda_R L_R$ affords the best spatial resolution in the Fig. 18 configuration. Thus we conclude that two-wavelength SPDC ghost imaging yields $\sim\sqrt{2}\bar{a}_L$ field-of-view in transverse coordinates and $\bar{\rho}_L$ spatial resolution. As in single-wavelength SDPC ghost imaging, the two-wavelength SPDC ghost image is inverted. In short, two-wavelength SPDC ghost imaging with $\lambda_S L_S = \lambda_R L_R$ performs the same as single-wavelength SPDC ghost imaging at wavelength λ_m and path length L_m for $m = S$ or $m = R$.

6 Conclusions

Our long journey through ghost imaging is now at its end. Building on solid foundational knowledge of classical and quantum Gaussian states, semiclassical versus quantum photodetection, and coherence propagation for phase-insensitive and phase-sensitive light, we have presented a unified treatment of SPDC and pseudothermal ghost imaging in lensless far-field operation. Moreover, we have gone beyond analysis alone by exhibiting two alternative but equally valid physical interpretations for ghost-image formation—correlations between the speckle patterns illuminating the high-spatial-resolution (reference) detector and the object to be imaged, and non-local two-photon interference—thus eliminating any residual controversy regarding the physics of ghost imaging.

To be specific, our conclusions as to the physics of ghost imaging are as follows. Pseudothermal ghost imaging can be understood as arising from correlations between classical speckle patterns cast on the object and the reference detector, *or* from two-photon interference between the fields illuminating the bucket and reference detectors. In particular, the field-of-view, spatial resolution, image contrast, and signal-to-noise ratio predictions of semiclassical photodetection and quantum photodetection coincide for pseudothermal ghost imaging. Hence we *cannot* regard the pseudothermal ghost image as a quantum effect, because quantum theory is not needed for its quantitative characterization. For SPDC ghost imaging, on the other hand, the situation

is different. Here quantum theory is necessary to quantify the resulting performance, because of the entangled nature of SPDC's signal and idler. For example, one can show that Bell inequalities are violated by certain quantum states that can be used to perform ghost imaging [54]. Furthermore, SPDC ghost imaging can be combined with matched filtering to accomplish a restricted class of object recognition at the single-photon level [55]. However, for far-field lensless ghost imaging, the principal distinction between SPDC and pseudothermal operation is that the former achieves high contrast in DC-coupled setups whereas the latter does not. One should *not* conclude from the preceding sentence that AC coupling, which suppresses the background term in the average pseudothermal ghost image, will eliminate all performance differences between classical-state and nonclassical-state ghost imaging: the shot noise and excess noise from the background term still affect the image signal-to-noise ratio in AC-coupled setups, see [30].

Finally, in this review we addressed recent extensions to the original ghost imaging paradigm: ghost imaging in reflection, ghost imaging through atmospheric turbulence, and two-wavelength ghost imaging. The book is far from closed, however, on ghost imaging. Its application to standoff sensing has only begun to be considered, see [23] for a preliminary spatial resolution and signal-to-noise ratio comparison with a cw laser radar. Furthermore, the connection between computational ghost imaging and compressive sensing opens up significant pathways for improving the standoff-sensing performance of ghost imaging. Indeed, a compressive-sensing ghost imaging in which the sequence of illumination patterns that are employed is adapted, as measurements are made, to maximize information gain would seem to be a natural topic for future research. Of course, standoff sensing is not the only possible application for ghost imaging, nor is the lensless, direct-detection configuration the only way to form ghost images. In particular, the use of higher-order correlations to form ghost images has been considered [32, 33, 56, 57] as has the use of homodyne detection instead of direct detection [58]. We feel confident that additional ghost imaging approaches will continue to be developed in the future.

References

1. Pittman, T.B., Shih, Y.H., Strekalov, D.V., Sergienko, A.V.: Optical imaging by means of two-photon quantum entanglement. *Phys. Rev. A* **52**, R3429–R3432 (1995)
2. Abouraddy, A.F., Saleh, B.E.A., Sergienko, A.V., Teich, M.C.: Role of entanglement in two-photon imaging. *Phys. Rev. Lett.* **87**, 123602 (2001)
3. Bennink, R.S., Bentley, S.J., Boyd, R.W.: “Two-photon” coincidence imaging with a classical source. *Phys. Rev. Lett.* **89**, 113601 (2002)
4. Gatti, A., Brambilla, E., Lugiato, L.A.: Entangled imaging and wave-particle duality: from the microscopic to the macroscopic realm. *Phys. Rev. Lett.* **90**, 133603 (2003)
5. Bennink, R.S., Bentley, S.J., Boyd, R.W., Howell, J.C.: Quantum and classical coincidence imaging. *Phys. Rev. Lett.* **92**, 033601 (2004)
6. Howell, J.C., Bennink, R.S., Bentley, S.J., Boyd, R.W.: Realization of the Einstein–Podolsky–Rosen paradox using momentum and position-entangled photons from spontaneous parametric down conversion. *Phys. Rev. Lett.* **92**, 210403 (2004)
7. Reid, M.D.: Demonstration of the Einstein–Podolsky–Rosen paradox using nondegenerate parametric amplification. *Phys. Rev. A* **40**, 913–923 (1989)
8. Gatti, A., Brambilla, E., Bache, M., Lugiato, L.A.: Correlated imaging, quantum and classical. *Phys. Rev. A* **70**, 013802 (2004)

9. Gatti, A., Brambilla, E., Bache, M., Lugiato, L.A.: Ghost imaging with thermal light: comparing entanglement and classical correlation. *Phys. Rev. Lett.* **93**, 093602 (2004)
10. Cai, Y., Zhu, S.-Y.: Ghost imaging with incoherent and partially coherent light radiation. *Phys. Rev. E* **71**, 056607 (2005)
11. Cai, Y., Zhu, S.-Y.: Ghost interference with partially coherent light radiation. *Opt. Lett.* **29**, 2716–2718 (2004)
12. Valencia, A., Scarcelli, G., D’Angelo, M., Shih, Y.: Two-photon imaging with thermal light. *Phys. Rev. Lett.* **94**, 063601 (2005)
13. Ferri, F., Magatti, D., Gatti, A., Bache, M., Brambilla, E., Lugiato, L.A.: High-resolution ghost image and ghost diffraction experiments with thermal light. *Phys. Rev. Lett.* **94**, 183602 (2005)
14. Scarcelli, G., Berardi, V., Shih, Y.: Can two-photon correlation of chaotic light be considered as correlation of intensity fluctuations?. *Phys. Rev. Lett.* **96**, 063602 (2006)
15. Erkmén, B.I., Shapiro, J.H.: Unified theory of ghost imaging with Gaussian-state light. *Phys. Rev. A* **77**, 043809 (2008)
16. Shapiro, J.H.: Computational ghost imaging. *Phys. Rev. A* **78**, 061802(R) (2008)
17. Shapiro, J.H.: The quantum theory of optical communications. *IEEE J. Sel. Top. Quantum Electron.* **15**, 1547–1569 (2009); Shapiro, J.H. Corrections to “The quantum theory of optical communications” *IEEE J. Sel. Top. Quantum Electron.* **16**, 698 (2010)
18. Erkmén, B.I., Shapiro, J.H.: Ghost imaging: from quantum to classical to computational. *Adv. Opt. Photon.* **2**, 405–450 (2010)
19. Meyers, R., Deacon, K.S., Shih, Y.: Ghost-imaging experiment by measuring reflected photons. *Phys. Rev. A* **77**, 041801(R) (2008)
20. Meyers, R.E., Deacon, K.S., Shih, Y.: Quantum imaging of an obscured object by measurement of reflected photons. *Proc. SPIE* **7092**, 70920E (2008)
21. Meyers, R.E., Deacon, K.S.: Quantum ghost imaging experiments at ARL. *Proc. SPIE* **7815**, 78150I (2010)
22. Cheng, J.: Ghost imaging through turbulent atmosphere. *Opt. Express* **17**, 7916–7921 (2009)
23. Hardy, N.D., Shapiro, J.H.: Ghost imaging in reflection: resolution, contrast, and signal-to-noise ratio. *Proc. SPIE* **7815**, 78150P (2010)
24. Hardy, N.D.: Analyzing and improving image quality in reflective ghost imaging. S.M. thesis, MIT (2011)
25. Bromberg, Y., Katz, O., Silberberg, Y.: Ghost imaging with a single detector. *Phys. Rev. A* **79**, 053840 (2009)
26. Katz, O., Bromberg, Y., Silberberg, Y.: Compressive ghost imaging. *Appl. Phys. Lett.* **95**, 131110 (2009)
27. Rubin, M.H., Shih, Y.: Resolution of ghost imaging for nondegenerate spontaneous parametric down-conversion. *Phys. Rev. A* **78**, 033836 (2008)
28. Chan, K.W.C., O’Sullivan, M.N., Boyd, R.W.: Two-color ghost imaging. *Phys. Rev. A* **79**, 033808 (2009)
29. Karmakar, S., Shih, Y.: Observation of two-color ghost imaging. *Proc. SPIE* **7815**, 78150R (2010)
30. Erkmén, B.I., Shapiro, J.H.: Signal-to-noise ratio of Gaussian-state ghost imaging. *Phys. Rev. A* **79**, 023833 (2009)
31. O’Sullivan, M.N., Chan, K.W.C., Boyd, R.W.: Comparison of the signal-to-noise characteristics of quantum versus thermal ghost imaging. *Phys. Rev. A* **82**, 053803 (2010)
32. Chan, K.W.C., O’Sullivan, M.N., Boyd, R.W.: High-order thermal ghost imaging. *Opt. Lett.* **34**, 3343–3345 (2009)
33. Chan, K.W.C., O’Sullivan, M.N., Boyd, R.W.: Optimization of thermal ghost imaging: high-order correlations vs. background subtraction. *Opt. Express* **18**, 5562–5573 (2010)
34. Wong, F.N.C., Kim, T., Shapiro, J.H.: Efficient generation of polarization-entangled photons in a nonlinear crystal. *Laser Phys.* **16**, 1517–1524 (2006)
35. Le Gouët, J., Venkatraman, D., Wong, F.N.C., Shapiro, J.H.: Classical low-coherence interferometry based on broadband parametric fluorescence and amplification. *Opt. Express* **17**, 17874 (2009)
36. Yuen, H.P., Shapiro, J.H.: Optical communication with two-photon coherent states—Part III: Quantum measurements realizable with photoemissive detectors. *IEEE Trans. Inf. Theory* **26**, 78–92 (1980)
37. Wozencraft, J.M., Jacobs, I.M.: Principles of Communication Engineering. pp. 205–206. Wiley, New York (1965)
38. Shapiro, J.H., Sun, K.-X.: Semiclassical versus quantum behavior in fourth-order interference. *J. Opt. Soc. Am. B* **11**, 1130–1141 (1994)

39. Mandel, L., Wolf, E.: *Optical Coherence and Quantum Optics*. Cambridge University Press, Cambridge (1995)
40. Shapiro, J.H., Shakeel, A.: Optimizing homodyne detection of quadratures-noise squeezing via local-oscillator selection. *J. Opt. Soc. Am. B* **14**, 232–249 (1997)
41. Saleh, B.E.A., Abouraddy, A.R., Sergienko, A.V., Teich, M.C.: Duality between partial coherence and partial entanglement. *Phys. Rev. A* **62**, 043816 (2000)
42. Erkmen, B.I., Shapiro, J.H.: Optical coherence theory for phase-sensitive light. *Proc. SPIE* **6305**, 63050G (2006)
43. Yuen, H.P., Shapiro, J.H.: Optical communication with two-photon coherent states—Part I: quantum state propagation and quantum noise reduction. *IEEE Trans. Inf. Theory* **24**, 657–668 (1978)
44. Shih, Y.: Quantum imaging. *IEEE J. Sel. Top. Quantum Electron.* **13**, 1016–1030 (2007)
45. Goodman, J.W.: *Speckle Phenomena in Optics: Theory and Applications*. Roberts & Co., Englewood, CO (2007)
46. Glauber, R.J.: Optical coherence and photon statistics. In: DeWitt, C., Blandin, A., Cohen-Tannoudji, C. (eds.) *Quantum Optics and Electronics*, Gordon and Breach, New York (1965)
47. Tatarski, V.I.: *Wave Propagation in a Turbulent Medium*. Dover Publications, New York (1961)
48. Strohbehn, J.W. (ed.): *Laser Beam Propagation in the Atmosphere*. Springer, Berlin (1978)
49. Ishimaru, A.: *Wave Propagation and Scattering in Random Media*. Vol. 2, Academic Press, New York (1978)
50. Shapiro, J.H., Capron, B.A., Harney, R.C.: Imaging and target detection with a heterodyne-reception optical radar. *Appl. Opt.* **20**, 3292–3313 (1981)
51. Dixon, P.B., Howland, G., Chan, K.W.C., O’Sullivan-Hale, C., Rodenburg, B., Hardy, N.D., Shapiro, J.H., Simon, D.S., Sergienko, A.V., Boyd, R.W., Howell, J.C.: Quantum ghost imaging through turbulence. *Phys. Rev. A* **83**, 051803(R) (2011)
52. Candès, E., Wakin, M.B.: Compressive sampling. *IEEE Signal Proc. Mag.* **25**, 21–30 (March 2008)
53. Duarte, M.F., Davenport, M.A., Takhar, D., Laska, J.N., Sun, T., Kelly, K.F., Baraniuk, R.G.: Single-pixel imaging via compressive sampling. *IEEE Signal Proc. Mag.* **25**, 83–91 (March 2008)
54. Jack, B., Leach, J., Romero, J., Franke-Arnold, S., Ritsch-Marte, M., Barnett, S.M., Padgett, M.J.: Holographic ghost imaging and the violation of a Bell inequality. *Phys. Rev. Lett.* **103**, 083602 (2009)
55. Malik, M., Shin, H., O’Sullivan, M., Zerom, P., Boyd, R.W.: Quantum ghost image discrimination with correlated photon pairs. *Phys. Rev. Lett.* **104**, 163602 (2010)
56. Liu, Q., Chen, X.-H., Luo, K.-H., Wu, W., Wu, L.-A.: Role of multiphoton bunching in high-order ghost imaging with thermal light sources. *Phys. Rev. A* **79**, 053844 (2009)
57. Ou, L.-H., Kuang, L.-M.: Ghost imaging with third-order correlated thermal light. *J. Phys B* **40**, 1833–1844 (2007)
58. Bache, M., Brambilla, E., Gatti, A., Lugiato, L.A.: Ghost imaging using homodyne detection. *Phys. Rev. A* **70**, 023823 (2004)